Maximum spreading of droplet-particle collision covering a low Weber number regime and data-driven prediction model

Ikroh Yoon, Jalel Chergui, Damir Juric, Seungwon Shin

Maximum spreading of droplet-particle collision covering a low Weber number regime and data-driven prediction model

Ikroh Yoon[1,2], Jalel Chergui[3], Damir Juric[3,4] and Seungwon Shin[5,a]

[1]Korea Institute of Marine Science and Technology Promotion (KIMST), Seoul, 06775 Korea, iryoon@kimst.re.kr

[2]Intergovernmental Oceanographic Commission of United Nations Educational, Scientific and Cultural Organization (UNESCO)

[3]Centre National de la Recherche Scientifique (CNRS), Laboratoire Interdisciplinaire des Sciences du Numérique (LISN), Université Paris Saclay, 91400 Orsay, France, Damir.Juric@limsi.fr, Jalel.Chergui@limsi.fr

[4]Department of Applied Mathematics and Theoretical Physics, University of Cambridge, Centre for Mathematical Sciences, Wilberforce Road, Cambridge CB3 0WA, UK

[5]Department of Mechanical and System Design Engineering, Hongik University, Seoul, 04066 Korea, sshin@hongik.ac.kr

[a)] Corresponding Author:
Professor Seungwon Shin, PhD

Phone: 82-2-320-3038

FAX: 82-2-322-7003

E-Mail: sshin@hongik.ac.kr

ABSTRACT

In the present study, the maximum spreading diameter of a droplet impacting with a spherical particle is numerically studied for a wide range of impact conditions: Weber number 0–110, Ohnesorge number 0.0013–0.7869, equilibrium contact angle 20°–160°, and droplet-to-particle size ratio 1/10–1/2. A total of 2600 collision cases are simulated to enable a systematic analysis and prepare a large dataset for training of a data-driven prediction model. The effects of four impact parameters on the maximum spreading diameter are comprehensively and quantitatively analyzed, focusing on the low Weber number regime. A universal model for prediction of β^*_{max} is also proposed based on a deep neural network. It is shown that our data-driven model can predict the maximum spreading diameter well, showing an excellent agreement with the existing experimental results as well as our simulation dataset within a deviation range of ± 10%.

Keywords: droplet impact; spherical particle; maximum spreading; multiphase flow; numerical simulation; artificial intelligence; deep neural network; data-driven prediction

I. INTRODUCTION

Droplet-particle interaction, one of the most common phenomena in nature, can be found in diverse engineering applications across various industrial fields such as inkjet printing,[1] medical diagnostics,[2] agricultural sprays,[3] cooling,[4] forensic analysis,[5] self-cleaning surfaces,[6] fluid catalytic cracking (FCC),[7] tablet coating in pharmaceutical industries,[8] to name a few examples. These fascinating collision phenomena are primarily driven by a complicated interplay and competition between capillary, inertial, and viscous forces during very small time and length scales.[9,10]

Researchers have extensively studied the pertinent physics underlying droplet collision with a solid surface. The fundamental process of droplet impact with a solid surface (impact – spreading – recoiling and, in some cases, followed by bouncing)[11,16] and roles of impact parameters (e.g., impact velocity and surface wettability, etc)[15,17,18] on the spreading behaviors and outcomes have come to light. In particular, many studies have been devoted to the maximal wetting area (which is generally characterized by using the maximum spreading diameter) owing to its practical importance.[11-15] Various prediction models for the maximum spreading including theoretical models[19,20] and empirical relations[11] have also been proposed and found to reproduce the experimentally observed maximum spreading diameters well for a wide range of impact conditions.[19]

Although many studies have been presented for the maximum spreading upon droplet collision with a flat surface,[11-14,19,20] few studies have focused on droplet impact with a curved surface (e.g., spherical particle), owing to the complex nature of the underlying physics.[21,22] Bakshi *et al.*,[23] Zhu *et al.*,[24] and Mitra *et al.*[25] investigated how the film thickness changes during droplet collision with a particle. It has been shown that the non-dimensional film

thickness measured at the apex point can be collapsed onto a single curve during certain periods,[23,25] and can be represented by a scaling expression.[24] The characteristics of lamella have also been investigated.[26-28] Banitabaei and Amirfazli[26,27] studied droplet collisions with a stationary[26] and a moving particle,[27] and analyzed various effects of collision conditions (e.g., impact velocity, surface wettability, and so forth) on structures and dynamics of the lamella for a broad range of collision conditions. Vilela and de Souza[36] used a machine learning approach to examine the effect of Weber number (We) and Reynolds number (Re) on the lamella structure. Yoon and Shin[29] and Dalgamoni and Yong[30] investigated droplet-particle collision, focusing on effects of Weber number, surface wettability and particle size on collision behaviors and impact outcomes. Seven collision scenarios mapped against the outcome regime maps,[29] and a theoretical model for droplet rebound criterion[30] have been presented. Malgarinos *et al*.,[31,32] Mitra et al.,[33] and Mitra and Evans,[34] studied droplet collisions with a particle focusing on heat transfer and phase change behavior during a collision process. Various effects of impact conditions on collision phenomena have been investigated in the film boiling regime mainly based on numerical simulations.[31-34] Even though these studies mentioned above have significantly shed light on our understanding of fundamental knowledge associated with droplet impact with a particle, they have mostly focused on the behaviors of film thickness, lamella structure, collision outcomes, heat transfer and phase change characteristics rather than on the maximal spreading of droplet-particle collision.

We now review recent work in the maximum spreading of droplet collision with a particle. Li and Wang,[35] Liu *et al*.,[36] Yoon and Shin,[37] and Khurana *et al*.[38] performed extensive parametric studies and analyzed effects of Weber number,[35-38] particle size[35-38] and surface wettability[36-38] on the maximum spreading of droplet-particle collision. In their study, how impact conditions can affect dynamic characteristics of a droplet's spreading and its

maximum values were analyzed for wide ranges of collision conditions. Several prediction models for the maximum spreading of droplet-particle collision have also been proposed.[36,38-42] Liu *et al*.,[36] Khurana *et al*.[38] and Mitra *et al*.[39] proposed theoretical models based on energy analyses to predict the maximum spreading and their models considered various effects of collision conditions, e.g., Weber number, Reynolds number, droplet-to-particle size ratio and surface wettability. However, those models[36,38] have been experimentally validated for only a very low liquid viscosity using a water droplet. Empirical models have also been proposed.[40-42] Khojasteh *et al*.[40] modified the existing correlations which were originally developed for impacts onto a flat surface and Bordbar *et al*.,[41] proposed an empirical model as a function of surface wettability and Weber number. However, they considered impacts only within a relatively narrow range of Weber number (5–30) on non-wettable surfaces (hydrophobic and super-hydrophobic).[40.41] Recently, Yoon and Shin[42] proposed an empirical correlation that can be applied to both a flat surface and a curved surface for a wide range of liquid viscosity, i.e., Ohnesorge (Oh) numbers up to the order of O(−1), but the effect of surface wettability was not incorporated.

Even considering the various studies heretofore undertaken, it still remains difficult to grasp comprehensively how the maximum spreading of a droplet impacting with a particle can be affected by various impact conditions. In particular, most studies have considered a range of sufficiently high Weber number, i.e., on the order of O(1) or higher. This means that existing studies have mainly focused on the inertia-driven spreading regime. However, in some applications such as inkjet printing technology, impact conditions for printable ink can reach very low Weber numbers, i.e., on the order of O(0).[30,43,44] A molten droplet can also undergo low Weber number collision in digital micro-fabrication technology to ensure a precise gentle deposition for fabrication of three-dimensional micro structures.[45] Despite its importance, only a few numerical studies[29,35,40,41,46] have considered droplet impact with a

particle for such a low Weber number regime (We ≤ 10). The effects of various collision parameters (e.g., droplet-to-particle size ratio, surface wettability, liquid viscosity, etc) still remain unclear. This implies the need for a systematic analysis focusing on the low Weber number regime.

Among others, it is difficult to predict the maximum spreading in a droplet-particle collision system using the existing prediction models[36,38,40-42] particularly for a low Weber number regime, because the existing models have been validated only with limited impact conditions, i.e., at relatively high Weber numbers (We > 10),[36,38,42] very low liquid viscosity[36,38,40,41] or only on non-wettable surfaces.[40-42] For example, some existing models[40-42] yield the value of zero for the maximum spreading where the impact velocity is zero (We = 0), which is physically unrealistic since a droplet can wet a solid surface by purely capillary effects without initial (inertial) impact energy.[13] It has been shown that the maximum spreading diameter of millimetric droplets can reach to about their initial droplet diameter, even though their impact velocities are zero.[13] This highlights the need for the development of new prediction model for the maximum spreading of droplet-particle collision systems available for the low Weber number regime, and surely, it would be ideal to have a universal model that can be applied to both the low and high Weber number regimes.

In this paper, we investigate the droplet-particle collision phenomena for both low and high Weber number regimes. To comprehensively understand how the maximum spreading differs from the high Weber number regime, various effects of important collision parameters (such as Weber number, surface wettability, liquid viscosity, and surface curvature of the particle) on the maximum spreading are systematically analyzed and quantitatively compared between those two regimes (i.e., low and high Weber number regimes). To propose a universal prediction model for the maximum spreading in droplet-particle collision systems that can be applied not only for both low and high Weber number regimes, but also for a wide

range of other important collision conditions, i.e., from low to high liquid viscosity, from a hydrophilic to a super-hydrophobic surface, and from a particle to a flat surface, a data-driven strategy is considered. The remainder of this paper is organized as follows: Section II briefly introduces the numerical methods used in the present study. Section III systematically analyzes the maximum spreading of a droplet colliding with a particle, and compares the effects of various collision conditions between two Weber number regimes. A data-driven prediction model is also proposed in this section. The key findings are summarized in Section IV.

II. NUMERICAL METHOD

Since this paper focuses on understanding the physical behavior of a droplet colliding with a particle and since we have used the same numerical methods as in our previous studies[42,47] here we briefly introduce the numerical formulations used in the current study. For more algorithm details and pertinent information on the numerical methods, readers can refer to the appendix and our previous papers.[42,47–49] Note that our simulation methods have been extensively applied to many droplet impact problems with various solid surfaces, e.g., flat surfaces,[50] cylindrical objects,[51] spherical targets,[29,37,42,47] and liquid pools.[52]

As a single field formulation, the governing equations are applied to all phases (gas, liquid, and solid) and are solved on the fixed Eulerian grid for incompressible flows:

$$\nabla \cdot \mathbf{u} = 0 \tag{1}$$

$$\rho\left[\frac{\partial \mathbf{u}}{\partial t} + \mathbf{u}\cdot\nabla\mathbf{u}\right] = -\nabla P + \rho\mathbf{g} + \nabla\cdot\mu\left(\nabla\mathbf{u} + \nabla\mathbf{u}^{\mathrm{T}}\right) + \mathbf{F} \tag{2}$$

where $\mathbf{u}$ is the velocity vector, P is the pressure, $\mathbf{g}$ is the gravitational acceleration, and ρ and μ are the density and the viscosity, respectively. $\mathbf{F}$ is the surface tension force which is considered only at the gas-liquid phase interface and can be described by the following formulation:

$$\mathbf{F} = \sigma\kappa_{\mathrm{H}}\nabla I \tag{3}$$

where σ is the surface tension coefficient and κ_H is the curvature field. The indicator function I has the characteristics of the Heaviside function and varies from 0 in one phase (droplet) to 1 in the other phase (air).

The physical properties of the gas (air) and liquid (droplet) can also be described using the indicator function I as follows:

$$\rho = \rho_d + (\rho_a - \rho_d) I \tag{4}$$

$$\mu = \mu_d + (\mu_a - \mu_d) I \tag{5}$$

where the subscripts "d" and "a" stand for droplet and air, respectively.

The level contour reconstruction method (LCRM)[48-50] is an essential element of our numerical framework to represent and track the phase interface. The LCRM is a hybrid interface-tracking method that benefits from both the front tracking[53] and the level set[54] methods. Although the interface is tracked using Lagrangian moving elements as in the original front tracking method for an accurate representation, each Lagrangian mesh element is naturally (implicitly) interconnected by reconstructing the elements based on the distance function. This reconstruction procedure eliminates the complexities in handling the element connectivity during the topology change of the phase interface (e.g., deformation, merging or pinch-off), which is the most well-known and significant shortcoming of the original front tracking, while keeping the advantage of the front-tracking method (i.e., interface representation using Lagrangian moving mesh elements). Since the reconstruction procedure is performed at the cell faces, mesh elements are implicitly connected after reconstruction without an additional treatment for linking the elements. More details about the LCRM can be found in Shin and Juric.[48-50]

Figure 1 shows the simulation geometry with boundary conditions applied in the present study. All simulations were performed in a two-dimensional axi-symmetric domain. The dimensions of the physical domain in the radial (r) and axial (z) directions are R_L = 7.5 and Z_L = 20 times the droplet radius, respectively. A droplet collides on a stationary, dry, spherical particle at an initial collision velocity V_{ini}, and D_d and D_p are the diameters of droplet and particle, respectively, where the subscript "p" stands for the particle. Ω is defined as the droplet-to-particle size ratio ($\Omega = D_d/D_p$). The axi-symmetric boundary condition is applied at the left boundary. At the upper, lower, and right boundaries, pressure boundary conditions are applied. The nondimensional spreading diameter (β^*) is defined as $\beta^* = \beta/D_d$ where β is the wetted arc length of the droplet (red arrow in Fig. 1). Its maximal value, i.e., the maximum spreading diameter is denoted β^*_{max}.

III. RESULTS AND DISCUSSION

Three dimensionless numbers, i.e., the Weber number (We = $\rho_d V_{ini}^2 D_d/\sigma$), the Ohnesorge number [Oh = $\mu_d/(\rho_d \sigma D_d)^{0.5}$], and the Reynolds number (Re = $\rho_d V_{ini} D_d/\mu_d$) are commonly used to characterize impact conditions for droplet collision with a solid surface. Since Oh can also be expressed using We and Re (Oh = $We^{0.5}$/Re), we here choose two dimensionless numbers, i.e., We and Oh as impact parameters. In the present study, in addition, two other impact parameters, i.e., the droplet-to-particle size ratio Ω and the equilibrium contact angle θ_{eqi} (which characterizes surface wettability) are also considered to cover a wide spectrum of collision conditions. We, Oh, and Ω are controlled by varying the impact velocity V_{ini}, liquid viscosity μ_d, and the particle diameter D_p, respectively.

The diameter of the droplet (D_d) is fixed to be D_d = 2 mm. For the gas phase, the physical properties of ambient air are used (ρ_a = 1.2 kg/m^3 and μ_a = 0.00018 N s/m^2). The surface tension coefficient is set as σ = 0.0728 N/m and the density of the liquid (droplet) is set to be ρ_d = 998.2 kg/m^3.

Since a droplet can splash on a stationary particle if the Weber number is We ~ 150, we consider a range of Weber numbers below this splashing threshold.[29,55] Seven We cases are considered for the low Weber number regime (We = 0, 1, 2, 4, 6, 8, and 10) and six cases are considered for the high Weber number regime (We = 20, 30, 50, 70, 90 and 110). Thus 13 cases of initial impact velocity (V_{ini}) are considered which vary from 0 to 2.003 m/s ($0 \le V_{ini} \le 2.003$) and thus varying the We number from 0 to 110 ($0 \le We \le 110$). To sufficiently cover the wide range of liquid viscosity, μ_d varies from 0.0005 to 0.3 N s/m^2 thus varying the Oh number from 0.0013 to 0.7869 ($0.0013 \le Oh \le 0.7869$), as in our previous study.[42] This range of Oh number almost covers many cases of practical interest across various engineering fields:

gasoline (Oh ~ 0.0018), water (Oh ~ 0.0026), ethyl alcohol (Oh ~ 0.0063), blood (Oh ~ 0.0063), squalane (Oh ~ 0.05), and printable ink (Oh ~ 0.1–1.0) with the given droplet diameter (D_d = 2 mm).[43,56]

The impact phenomena observed in droplet-particle collisions can be identical to that on a flat surface if the particle is sufficiently large. Because no notable difference in the maximum spreading diameter (β^*_{max}) between a flat surface and a particle was observed when the particle size is larger than 10 times the droplet size,[36,42] it is assumed that the collision case where Ω = 1/10 produces an identical result to an impact with a flat surface.[36,42] On the other hand, β^*_{max} cannot be defined since the droplet can completely wet the particle (the particle surface can be totally coated by the droplet) if the particle is sufficiently small. It has been shown that such complete coating can be observed near Ω = 1/1.5.[29,38] Therefore, four cases of Ω (Ω = 1/10, 1/4, 1/3, and 1/2) are considered herein to investigate the effect of particle size on the maximum spreading characteristics covering the critical range of Ω. Five cases of θ_{eqi} are also considered to examine the effect of surface wettability from hydrophilic to super-hydrophobic surfaces, i.e., θ_{eqi} = 20°, 55°, 90°, 125° and 160°. As a result, a total of 2600 collision cases (13 Weber numbers, 10 Ohnesorge numbers, 4 droplet-to-particle size ratios, and 5 surface wettabilities) are considered in our current simulations. This large dataset is used not only to understand how β^*_{max} changes across two regimes (low and high Weber number regimes) regarding the effects of other impact parameters (Oh, Ω, and θ_{eqi}) but also to train an artificial neural network to develop a data-driven prediction model for β^*_{max} as a universal predictor (a more detailed description of this artificial neural network is presented in Section III C).

We assume that the surface is well-prepared thus the contact angle hysteresis is set as ±2.5°. Since the Reynolds number is on the order of O(4) or smaller and this is too small to consider turbulence[57], the flow is assumed as laminar flow. The deformation of the droplet

before collision can also be negligible.[38] To set the desired impact velocity V_{ini} before the impact, the droplet is accelerated artificially by solving the governing equations under an enhanced gravity field without interface advection.

A. Validations

While our numerical framework has been extensively validated for a wide range of collision conditions,[29,42] additional validation tests have been performed to check that the numerical methods used herein can simulate the droplet-particle impact phenomena well focusing on the low Weber number regime. A water droplet (Oh=0.0026) is used to show our result hereafter for its versatility, unless otherwise mentioned.

Figure 2(a) shows the temporal variation of the nondimensional spreading diameter (β^*) for a flat surface (Ω = 1/10) when the initial impact velocity is zero. Two different surfaces, i.e. steel (θ_{eqi} = 61°, as a hydrophilic surface) and parafilm (θ_{eqi} = 110°, as a hydrophobic surface) are considered. As mentioned above, and as also shown by the experiment of Lee *et al*.,[13] the droplet spreads over the solid surface by only the capillary effect, thus β^*_{max} yielding zero is physically unrealistic. Note that the interaction phenomena between droplet and particle is primarily governed by the capillary effect without the (initial) inertial effect under the given impact condition (We = 0). The measured β^*_{max} in our simulations (marked by black and red crosses) show a good agreement with existing experimental results (indicated by two dashed lines).[13]

We further compare our simulation result with the existing experimental result of Mitra *et al*.[25] to check that our simulation method can reproduce the droplet spreading well on a curved surface, i.e., spherical particle. Note that low Weber number (We = 0.9) and high particle curvature (Ω = 0.83) are considered. In figure 2(b) and 2(c), the temporal evolutions

of β^* and the apparent contact angle (θ_{ap}) are compared with the existing experimental result, and our simulation result shows a good agreement with the experiments.[25] Although a small discrepancy is observed due to the difficulties in ensuring the exact head-on collision in the experiment,[25] we concluded that our numerical formulations perform reasonably well in simulating the droplet-particle collision problem for a low Weber number regime. Note again that our simulation framework has also been extensively validated in the high Weber number regime (We ~ 155.5),[29] and for a wide range of Oh numbers ($0.0013 \leq Oh \leq 0.7869$).[42]

B. Comprehensive analysis of the maximal spreading for low and high Weber number regimes

We first examine how β^*_{max} differs for the low Weber number regime from that for the high Weber number regime, and how the Weber number and surface wettability affect β^*_{max} for each regime. In figure 3, β^*_{max} is plotted for the full ranges of We and θ_{eqi} considered herein ($0 \leq We \leq 110$ and $20° \leq \theta_{eqi} \leq 160°$). As expected, β^*_{max} basically increases with We due to its higher inertial (impact) energy. However, a clear difference is observed between the high and low Weber number regimes. When the Weber number is sufficiently high ($We \geq 30$), the spreading is mainly governed by the inertial effect and β^*_{max} can be represented by the well-known scaling relation ($\beta^*_{max} \sim We^{0.25}$, see green dashed line)[12] for all considered surface wettabilities. Although β^*_{max} is still affected by θ_{eqi} because the capillary effect plays a non-negligible role near the maximum spreading state at which the velocity of the contact line decelerates and reaches zero,[15] the effect of θ_{eqi} is minor and the scaling relation can approximate β^*_{max} well. Conversely, the scaling relation doesn't hold for the low We regime. As We decreases, β^*_{max} diverges from the green dashed line depending on θ_{eqi}. Only β^*_{max} with the most non-wettable surface ($\theta_{eqi} = 160°$) can be approximated by the scaling relation.

In particular, a significant effect of the surface wettability is observed for this regime, which signifies that the maximum spreading is primarily governed by the capillary effect due to the low impact inertial energy. Note that β^*_{max} with $\theta_{eqi} = 20°$ is almost double the case with $\theta_{eqi} = 160°$, if We = 1. Note also that β^*_{max} converge to non-zero values depending on the surface wettatilbites if We reaches zero. This highlights again the limitation of some existing prediction models[40-42] that yield $\beta^*_{max} = 0$ when We = 0, for such a low Weber number regime.

Next, we examine how the droplet-to-particle size ratio (Ω) affects β^*_{max} and how the effect of Ω on β^*_{max} depends on the Weber number. In figure 4, β^*_{max} is compared for the full ranges of We and Ω considered herein ($0 \leq We \leq 110$ and $1/10 \leq \Omega \leq 1/2$). If the Weber number is sufficiently high ($We \geq 30$), as shown in many existing studies,[24,35-36,38,40-41] β^*_{max} increases on smaller particles and can also be approximated well by the existing scaling relations[12,42] (see two green dashed lines). Conversely, for the low We regime, the inverse trend is seen, i.e., β^*_{max} decreases on smaller particles (see $We \leq 4$ for this case) whereas the effect of Ω on β^*_{max} almost disappears at the transition regime (see $4 < We < 6$ for this case). We found that the transition regime is observed near $4 \leq We \leq 10$ depending on the surface wettability and β^*_{max} is nearly independent of Ω in this transition regime. We note that such a trend shown in the transition and low We regime ($We \leq 10$) is also consistent with the existing studies.[29-30,35-36,58]

In figures 3 and 4, we analyzed the effects of We, θ_{eqi} and Ω on β^*_{max} where the droplet is water (Oh = 0.0026). We now examine how those behaviors change if the liquid viscosity (i.e., Oh number) changes. In figure 5, the effect of surface wettability ($\theta_{eqi} = 20°$, 90°, and 160°) is compared for the full range of Oh considered herein ($0.0013 \leq Oh \leq 0.7869$). Two representative Weber number cases (We = 4 for the low We regime and We = 110 for the high We regime) are plotted for comparison. As expected, β^*_{max} basically decreases as Oh increases due to its higher viscous damping. For the high We cases (We = 110), β^* is

apparently affected by θ_{eqi} at the low Oh regime since the physical mechanism for the termination of spreading is related to the capillary effect and surface wettability. For this case (i.e., high We and low Oh), the droplet spreading is driven by the inertia and terminated by the capillary limit (i.e., the droplet can spread over the surface until no more interfacial deformation is available).[12,59] The effect of viscous damping on β^*_{max} can be minor for this case. However, as Oh increases, the viscous dissipation starts to play an important role, and for the cases with high We and high Oh, the droplet spreading is driven by the inertia and terminated by the viscous limit (i.e., the droplet can spread over the surface until no more kinetic energy is available).[12,59] Since the physical mechanism is not strongly related to the capillary effect at this high We and high Oh regime, the effect of θ_{eqi} on β^*_{max} is minor. Conversely, for the low We cases (We = 4), β^*_{max} is always affected by θ_{eqi} and a significant effect of θ_{eqi} is still observed even for the highest Oh case considered herein (Oh = 0.7869 which is 300 times more viscous compared to a water droplet). This means that the capillary effect and surface wettability play an important role in the droplet spreading for the low We cases, even though the liquid viscosity is significantly increased.

In figure 6, the effect of droplet-to-particle size ratio (Ω = 1/10 and 1/2) is compared for the full range of Oh considered herein ($0.0013 \leq Oh \leq 0.7869$). At the low Oh regime, as shown in figure 4, three different effects of Ω on β^*_{max} are seen depending on the Weber number: (i) β^*_{max} increases with Ω for the high We case (We = 110), (ii) no effect of Ω on β^*_{max} appears for the transition regime case (We = 6), and (iii) β^*_{max} decreases as Ω increases for the very low We case (We = 1). For the high Oh regime, however, all of these effects of Ω on β^*_{max} become negligible as Oh increases since the deformation of the droplet itself is significantly suppressed due to its high viscous damping.

With regard to the effects of Ω on β^*_{max} and associated physical mechanisms, our results shown in figures 4 and 6 are consistent with many previous studies.[24,29-30,35-36,38,40-41,58] The

several underlying mechanisms, i.e., gravitational effect,[36] reduced surface energy loss[42] and reduced viscous dissipation,[38,42] have been investigated and proposed to explain why β^*_{max} increases on smaller particles for the high We regime. However, no detailed explanation is yet available about the physical mechanism for the transition and low We regime, even though the same trend has been found in the several existing studies.[29-30,35-36,58] In figure 7, we analyze how the surface energy and interfacial shapes are affected by Ω in more detail for the cases with We = 1. The surface energy of a droplet can be described as $E_s = \sigma[A_{LG} - A_{LS}\cdot\cos\theta_{eqi}]$ if a droplet is in contact with a solid. Here, A_{LG} and A_{LS} are the liquid-gas interfacial area and the wetting area (liquid-solid contact area), respectively, thus the term σA_{LG} denotes the liquid-gas interfacial energy and the term $\sigma A_{LS}\cdot\cos\theta_{eqi}$ is associated with the capillary effect acting in the vicinity of the contact line which essentially depends on the surface wettability. In figure 7(a), temporal evolutions of these two surface energy components, i.e., $E_{s(L/G)}$ and $E_{s(L/S)}$ with the total surface energy are plotted against the nondimensional time τ (defined as $\tau = tV_{ini}/D_d$) for the two different sizes of target particles (Ω = 1/2 and 1/4). All components are normalized by the initial (total) surface energy $E_{s,\,ini}$. For both cases, the droplets reach the maximum spreading state near $\tau \sim 0.63$ (see green dashed line). The total surface energy is slightly increased on the smaller particle, and this can be attributed to the reduced viscous dissipation on the smaller target. Since the smaller target provides higher surface curvature, the liquid-gas interface of the droplet should be essentially more stretched. This explains why $E_{s(L/G)}$ increases on the smaller particle (compare two dotted lines). Therefore, $E_{s(L/S)}$, which shows basically the same trend as the wetting area and the maximum spreading diameter, decreases on the smaller particle under the given total surface energy state (compare two dashed lines). In figure 7(b), the liquid-gas interface and the liquid-solid contact interface are further compared for the same cases shown in figure 7(a). As depicted in the zoom-in of the dotted box, the liquid-gas interfacial area is

larger on the smaller particle (see blue line) compared to that on the larger particle (see red line) whereas the wetting area is smaller on the smaller particle (see yellow line) compared to that on the larger particle (see green line).

We now compare temporal evolutions of the spreading characteristics between the high and low Weber number regimes. Two representative Weber number cases (We = 4 and 110) and Ohnesorge number cases (Oh = 0.0026 and 0.5246) are selected for comparison. In figure 8(a) and (b), the temporal variations of β^* against the nondimensional time τ for high (We = 110) and low (We = 4) Weber number cases are analyzed, respectively. The maximum spreading time (τ_{max}), assumed as the time at which the droplet attains 95 % of its maximum spreading (β^*_{max}), is marked by squares. As seen in figure 8(a), for the high We cases, although β^*_{max} and τ_{max} are still affected by the surface wettability, their effects are relatively minor. It is interesting to observe the initial period ($0 \leq \tau \leq 1$) at which the evolution of β^* shows an identical profile regardless of θ_{eqi}, under the given Oh condition (see green area). At this period, no capillary effect appears due to the dominant effect of high inertia. Such a result is also consistent with existing studies[23,25] that found that the nondimensional film thickness measured at the apex point shows an identical trend during certain initial periods, referred to as the 'initial deformation period ($0 \leq \tau \leq 0.7$)'. The effect of θ_{eqi} starts to play a role only after $\tau = 1$ for both Oh conditions. Conversely, as seen in Figure 8(b), the effect of θ_{eqi} obviously appears during the entire spreading process for low We cases. No initial period at which β^* shows an identical profile is seen. The effect of θ_{eqi} plays a significant role in both β^*_{max} and τ_{max}. For example, for the cases with Oh = 0.0026, τ_{max} on the hydrophilic surface ($\theta_{eqi} = 20°$) is 1.17 which is more than double τ_{max} (0.46) on the hydrophobic surface ($\theta_{eqi} = 160°$).

In figure 9, interfacial morphologies of the droplets at the maximum spreading state are compared in detail. 4 cases shown in figure 8 above are selected for comparison (We = 4 and

110, θ_{eqi} = 20° and 160°, and Oh = 0.0026). For high We cases, as seen in the left side of figure 9, the thin liquid film of lamella is observed at the central part of the droplet (see the right side of the green dashed line) whereas the rounded rim is formed at the leading part near the contact line due to the surface tension force (see the left side of the green dashed line). The interfacial morphologies are globally comparable for both surface wettabilities and an almost identical shape is observed for the lamella part. No meaningful difference in the film thickness as well as in the lamella shape is seen depending on θ_{eqi}. For these high We cases, only the local shape of the rims is affected by θ_{eqi}. Conversely, for the low We cases, it is difficult to distinguish clearly between the lamella and rim. As seen in the right side of figure 9, the interfacial shape is significantly affected by the surface wettability, across this entire part of the droplet. Relatively uniform film thickness is seen on the hydrophilic particle (θ_{eqi} = 20°) whereas the droplet shows a very thick and rounded shape on the non-wettable particle (θ_{eqi} = 160°). For this hydrophobic case (θ_{eqi} = 160°), a much reduced β^*_{max} is also seen compared to the case with θ_{eqi} = 20°.

C. Data-driven prediction model for the maximum spreading diameter

In Section III B above, we observed the highly complex nature of the physical process underlying the maximum spreading of droplet-particle collision. If the Weber number decreases below order of O(1), the existing scaling relations do not hold and the maximum spreading strongly depends on the surface wettability and the associated capillary effect even for the highly viscous cases (with high Oh numbers). In addition, the effect of the droplet-to-particle size ratio changes across the Weber number, and in some cases, shows the inverse trend at the low Weber number regime. Those complex behaviors also change nonlinearly as the Ohnesorge number changes. Overall, inertial, capillary, and viscous effects and surface

wettability all play non-negligible roles in β^*_{max} and their effects are complicatedly interconnected showing nonlinear characteristics.

A single correlation that can be applied to a wide range of collision conditions regarding all such complex effects from We, Oh, θ_{eqi}, and Ω is extremely difficult to formulate, even for a flat surface, since the different physical spreading mechanisms should be simultaneously considered.[15,19] Therefore, no single universal prediction model for the maximum spreading in the droplet-particle collision problem has yet been proposed.

Recently, machine learning approaches have been widely applied to complicated fluid flow phenomena[60-66] owing to their excellent ability as a universal correlator for non-linear relations between input and output data.[61] In particular, deep learning which utilizes "deep" layers to represent complex and nonlinear relations that are generally difficult to capture by using traditional methods have been increasingly applied to multiphase flow problems[66] (see Ref. 66 and references therein). In this section, we propose a data-driven prediction model for the maximum spreading of droplet-particle collision, using a deep learning approach.

β^*_{max} can be basically modeled as a function of 4 collision parameters:

$$\beta^*_{max} = f(\text{We}, \text{Oh}, \theta_{eqi}, \Omega) \tag{6}$$

The multilayer perceptron (MLP),[67] also called multilayer neural network, is used as a nonlinear regressor to represent the function f which is a complex relationship between input (We, Oh, θ_{eqi}, and Ω) and output (β^*_{max}) data in the present study. Figure 10 depicts the schematic architecture of the MLP considered in the present study, which consists of input layer, multiple hidden layers, and output layer. A number of neurons (also called nodes) exist in each layer. The input layer provides the input features (i.e., We, Oh, θ_{eqi}, and Ω in the current study) to the first hidden layer. In the first hidden layer, the linear combinations of the

input features are constructed and forwarded to the next hidden layer after nonlinearization by an activation function. This operation (so-called feedforward procedure) is continued over all of the layers and the last output layer predicts the final output value. The output value of the n^{th} neuron in the m^{th} layer can be described:

$$a_n^m = g\left(\sum_{k=1}^{N^{m-1}} w_{nl}^m a_l^{m-1} + b_n^m\right) \tag{7}$$

where N denotes the number of neurons of each layer whereas w_{nl} denotes the weight between the n^{th} neuron of the current layer and l^{th} neuron of the previous layer. b denotes the bias and the function g is the nonlinear activation function. More detailed information on the feedforward procedure can be found in the appendix B.

A total of 2600 simulation cases are used to prepare the dataset: 13 cases of Weber numbers (We = 0, 1, 2, 4, 6, 8, 10, 20, 30, 50, 70, 90, and 110), 10 cases of Ohnesorge numbers (Oh = 0.0013, 0.0026, 0.0052, 0.0105, 0.0262, 0.0525, 0.1049, 0.2623, 0.5246, and 0.7869), 5 cases of surface wettabilities (θ_{eqi} = 20°, 55°, 90°, 125° and 160°), and 4 cases of droplet-to-particle-size ratios (Ω = 1/10, 1/4, 1/3, and 1/2). The simulations have been efficiently performed with the help of a simple adaptive mesh refinement (AMR) technique.[47] From those simulation cases, 2600 data samples for input features (We, Oh, θ_{eqi}, and Ω) and output feature (β^*_{max}) are constructed. Afterward, the dataset is randomly divided into 3 parts: the training data (70 %, 1820 data samples), the validation data (15 %, 390 data samples), and the test data (15 %, 390 data samples). The training data is used to train the deep neural network model whereas the validation data is used to check if overfitting happens during the learning process. The trained model is finally tested using the test dataset.

The adjustable coefficients, i.e., weights (w) and biases (b) of the MLP are optimized

during the learning process, by minimizing the loss function using the back propagation algorithm.[68] In the present study, the mean square error (MSE) is defined and applied as a loss function:

$$\mathrm{MSE} = \frac{1}{M}\sum_{k=1}^{M}\left(\beta^*_{\max} - \beta^*_{\max(\mathrm{p})}\right)^2 \tag{8}$$

Where M denotes the number of data samples and $\beta^*_{\max(\mathrm{p})}$ denotes the predicted value of the maximum spreading diameter using the deep neural network. The number of hidden layers, the number of neurons at each layer, and the nonlinear activation function are called hyperparameters, and can usually be set by the user. In the present study, the rectified linear unit function, i.e., ReLU function is used as the activation function since the ReLU is known as the best candidate for deep neural networks.[69] The ReLU function is described as:

$$g(x) = \mathrm{ReLU}(x) = \max(x, 0) \tag{9}$$

Based on a 'trial and error' approach, a 2 × 30 (2 hidden layers and 30 neurons in each hidden layer) structure is selected as our MLP network. The training is performed by using the ADAM[70] optimization algorithm due to its well-known performance for deep learning applications.[71] All implementation for the training is performed in the open-source software library TensorFlow[72] and Keras.[73] Further detailed information about the MLP and its training techniques can also be found in Nielsen.[74]

The training of the neural network is performed until the MSE obtained from the validation dataset convergences to a steady state. After 4500 training epochs, the training and validation MSE reach a steady state at about 6.5×10^{-4} (training) and 2.5×10^{-3} (validation),

respectively. The final MSE of the test dataset is 9.7×10^{-4}.

Figure 11 compares the maximum spreading of droplet-particle collision predicted by our deep neural network with the measured values (true values) from our numerical simulations. 390 data samples of the test dataset are used for comparison (see black circles). As seen, β^*_{max} predicted by our deep neural network model shows an excellent agreement with the true (measured) data (R^2 = 0.9968). Note that only 1 of 390 cases falls outside a deviation range of ± 10%. We also plot 4 existing results together, i.e., two experimental results for the droplet-particle collisions,[25,38] the semi-empirical model[11] and the scaling model[12] for collisions with a flat surface for comparison. For droplet collision with a flat surface, the semi-empirical model of Mao *et al.*[11] is known as one of the most accurate models[75] and our data-driven prediction result also shows a good agreement with their model except for some cases (see red inverse triangles). This discrepancy is caused by the existing model's own limitation[11,75] that tends to somewhat overestimate the maximum spreading for the cases where the liquid viscosity is small thus the surface tension plays an important role. Since a viscosity-free model is more appropriate[14] for such impact conditions (i.e., low liquid viscosity), we compare our result again with the well-known viscosity-free model of Clanet *et al.*[12] and an excellent agreement is observed (see yellow squares). Our predicted β^*_{max} is also consistent with two other existing results for droplet collisions with a particle (see blue crosses and green triangles).[25,38] Note that all the data shown in figure 11 has not been used for the training of our deep neural network. This means that our data-driven prediction model can predict β^*_{max} well without overfitting. Note also that the current model is not a fully optimized version because detailed fitting and optimization of the deep neural network are beyond the scope of the present study. Indeed, we performed several model tests and found that the prediction performance can also be further improved using a 'deeper' network. However, we concluded that the current model is sufficiently reasonable in terms of its

accuracy and simplicity. Further optimization can be considered in future studies with additional larger datasets. The trained coefficients, i.e., weights (w) and biases (b), and more detailed feedforward procedure for the prediction of β^*_{max} using the current MLP model are presented in the appendix B for readers.

IV. CONCLUSION

In this study, we investigate the maximum spreading diameter (β^*_{max}) of droplet impact with a spherical particle for a wide range of impact conditions, i.e., from the low Weber number regime dominated by capillary effects to the high Weber number regime dominated by inertial effects ($0 \leq We \leq 110$), from nearly inviscid liquid to highly viscous liquid ($0.0013 \leq Oh \leq 0.7869$), from hydrophilic to super-hydrophobic surfaces ($20° \leq \theta_{eqi} \leq 160°$), and from a flat surface to a small particle ($1/10 \leq \Omega \leq 1/2$). A total of 2600 collision cases are simulated not only to enable a systematic analysis, but also to prepare a large dataset for the training of a data-driven prediction model based on a deep neural network.

The effects of four impact conditions (We, Oh, Ω and θ_{eqi}) on β^*_{max} are comprehensively analyzed and quantitatively compared for both high and low Weber number regimes. For the low We regime, β^*_{max} cannot be predicted by the existing scaling relations, and strongly depends on the surface wettability (θ_{eqi}) and the associated capillary effect even for the highly viscous cases (with high Oh numbers). In addition, the effect of the droplet-to-particle size ratio (Ω) changes depending on the Weber number, i.e., β^*_{max} increases with Ω for the high We regime whereas β^*_{max} shows the inverse trend for the low Weber number regime. Those complex behaviors also nonlinearly change depending on the Ohnesorge number. The dynamic profile of β^* as well as interfacial shapes also significantly differ from those for the high We regime.

Finally, to consider all such complex and inter-related effects from four impact parameters (We, Oh, Ω and θ_{eqi}) simultaneously, a universal model for prediction of β^*_{max} is proposed based on a deep neural network. It is shown that our data-driven model can reproduce β^*_{max} well, showing an excellent agreement with the existing experimental results as well as our

simulation dataset.

ACKNOWLEDGMENTS

This work is supported by Basic Science Research Program through the National Research Foundation of Korea (NRF) funded by the Ministry of Education (2017R1D1A1B03028518) and by the National Research Foundation of Korea (NRF) through grants funded by the Korean government (MSIT) (2020R1A2C1003822) and support through computing time at the Institut du Developpement et des Ressources en Informatique Scientifique (IDRIS) of the Centre National de la Recherche Scientifique (CNRS), coordinated by GENCI (Grand Equipement National de Calcul Intensif) Grant 2022 A0122B06721.

APPENDIX A: Details of numerical method

We describe the essential parts of our numerical framework here, e.g., the calculation of the surface curvature, interface advection, and the modeling of the dynamic contact angle. In Eq. (3), the curvature field κ_{H} can be obtained as follows:

$$\kappa_{\mathrm{H}} = \frac{\mathbf{F}_{\mathrm{L}} \cdot \mathbf{G}}{\sigma \mathbf{G} \cdot \mathbf{G}} \tag{A1}$$

$$\mathbf{F}_{\mathrm{L}} = \int_{\Gamma(t)} \sigma \kappa_{\mathrm{f}} \mathbf{n}_{\mathrm{f}} \delta\left(\mathbf{x} - \mathbf{x}_{\mathrm{f}}\right) \mathrm{d}s \tag{A2}$$

$$\mathbf{G} = \int_{\Gamma(t)} \mathbf{n}_{\mathrm{f}} \delta\left(\mathbf{x} - \mathbf{x}_{\mathrm{f}}\right) \mathrm{d}s \tag{A3}$$

Here, $\mathbf{x}_{\mathrm{f}}$ is the position of the moving liquid-gas interface $\Gamma(t)$, which is tracked by the Lagrangian mesh elements. κ_{f} is also the curvature of the phase interface but is calculated using the Lagrangian elements directly. $\mathbf{n}_{\mathrm{f}}$ is the unit normal vector from the phase interface, and $\delta(\mathbf{x}\text{-}\mathbf{x}_{\mathrm{f}})$ is the Dirac delta function, which is non-zero only at the interface ($\mathbf{x} = \mathbf{x}_{\mathrm{f}}$). d$s$ is the length (in a two-dimensional simulation) of each interface element and is calculated directly from the interface elements.

The Lagrangian mesh elements are advected in time by integrating:

$$\frac{d\mathbf{x}_{\mathrm{f}}}{dt} = \mathbf{u}_{\mathrm{f}} \tag{A4}$$

where $\mathbf{u}_f$ is the velocity of each interface element. The second-order Runge-Kutta method is utilized for integrating Eq.(A4). For an element which is not in contact with a contact line, $\mathbf{u}_f$ is obtained using an appropriate interpolation scheme from the velocity field. Conversely, if an element is in contact with a solid surface, the element is advected by the Navier-slip condition to prevent a stress singularity which arises at the solid surface. In such a case, the velocity of the contact line (U_{CL}) on the surface is obtained by:

$$U_{CL} = \lambda \left\{ \frac{\partial \mathbf{u}}{\partial \mathbf{n}} \right\}_{wall} \tag{A5}$$

where λ is the proportionality slip constant and a quarter of the size of a grid cell is applied in the present study. $\partial\mathbf{u}/\partial\mathbf{n}$ is the shear strain rate on the wall.

The dynamic contact angle θ_{dyn} is modeled as in Yokoi *et al.*:[76]

$$\theta_{dyn}\left(U_{CL}\right) = \begin{cases} \min\left[\theta_{eqi} + \left(\dfrac{\mathrm{Ca}}{q_1} \right)^{1/3},\ \theta_{mda} \right], & \text{if } U_{CL} \geq 0 \ \text{ (for spreading)} \\ \max\left[\theta_{eqi} + \left(\dfrac{\mathrm{Ca}}{q_2} \right)^{1/3},\ \theta_{mdr} \right], & \text{if } U_{CL} \leq 0 \ \text{ (for receding).} \end{cases} \tag{A6}$$

where θ_{eqi} is the equilibrium contact angle and Ca is the capillary number ($\mathrm{Ca} = \mu U_{CL}/\sigma$). The contact angle hysteresis can be represented by the difference between the allowable maximum (θ_{mda}) and minimum (θ_{mdr}) dynamic contact angles. q_1 and q_2 are constants which can be experimentally measured. The same values as in Yokoi *et al.*[76] ($q_1 = 9.0 \times 10^{-9}$ and $q_2 = 9.0 \times 10^{-8}$) are used in the current study.

APPENDIX B: Feedforward procedure and the coefficients of the neural network model

The input data a^0 is first provided from the input layer in the form of a 1 × 4 matrix containing four input features (We, Oh, θ_{eqi}, and Ω). At the first hidden layer, the matrix multiplication between a^0 (1 × 4 matrix) and the weights of the first hidden layer w^1 (4 × 30 matrix), i.e., $a^0 \times w^1$ is performed, followed by adding the biases of the first hidden layer b^1 (1 × 30 matrix). The output of this procedure is nonlinearized by the rectified linear unit (ReLU) function before transmission to the next layer. The output of the first hidden layer a^1 can be expressed as $a^1 = \text{ReLU}\,[(a^0 \times w^1) + b^1]$ and has the form of a 1 × 30 matrix.

At the second hidden layer, the same procedure is applied. The matrix multiplication between a^1 (1 × 30 matrix) and the weights of the second hidden layer w^2 (30 × 30 matrix) is performed, followed by adding the biases of the second hidden layer b^2 (1 × 30 matrix) and nonlinearization by the ReLU function. The output of the second hidden layer a^2 can be expressed as $a^2 = \text{ReLU}\,[(a^1 \times w^2) + b^2]$ and has the form of a 1 × 30 matrix.

At the output layer, the same procedure is applied but the nonlinearization is not applied. The matrix multiplication between a^2 (1 × 30 matrix) and the weights of the output layer w^3 (30 × 1 matrix) is performed, followed by adding the biases of the output layer b^3 (1 × 1 matrix). The output of the output layer a^3, which is essentially the prediction result, can be expressed as $a^3 = (a^2 \times w^3) + b^3$.

TABLE B.1. Weights of the first hidden layer $w^1_{i,j}$ (4 × 30 matrix).

	$i = 1$	$i = 2$	$i = 3$	$i = 4$
$j = 1$	1.9061	-1.2706	0.0059	-1.5021
$j = 2$	2.4251	0.079	-0.0469	-4.0555
$j = 3$	-1.1888	0.1675	0.0157	-1.1465
$j = 4$	-2.3407	0.0191	0.0032	10.0215
$j = 5$	1.1278	-0.1337	0.0628	4.8798
$j = 6$	-0.2123	-0.1366	-0.0261	3.4507
$j = 7$	3.8299	0.0024	-0.0468	-19.7693
$j = 8$	1.4675	0.007	-0.0025	-36.5083
$j = 9$	0.1276	-0.0879	-0.3978	0.2503
$j = 10$	0.9491	-1.7436	0.0185	-0.6988
$j = 11$	-0.3328	-0.2501	-0.3118	0.0356
$j = 12$	0.3453	0.0053	-0.0739	0.3906
$j = 13$	0.1566	-0.3271	-0.236	0.0934
$j = 14$	0.8228	-0.4258	0.0497	-4.1911
$j = 15$	-0.2457	-0.2498	-0.1976	0.3705
$j = 16$	-2.7326	-0.0792	0.0164	-1.6066
$j = 17$	4.4666	-0.0969	0.0141	2.9657
$j = 18$	-0.1839	-0.2803	-0.3558	0.3828
$j = 19$	-4.678	0.0082	0.0005	-5.5569
$j = 20$	0.1821	-0.4191	-0.0108	-2.9936
$j = 21$	-0.2881	-0.395	-0.0686	-0.1405
$j = 22$	1.9539	0.02	-0.003	-17.0311
$j = 23$	-6.5675	0.0344	-0.0017	2.8008
$j = 24$	-1.7524	-0.4745	-0.0399	1.2429
$j = 25$	3.4064	-0.0234	0.0057	-1.134
$j = 26$	-0.233	-0.1278	-0.0119	0.3623
$j = 27$	-0.326	0.0482	-0.2477	-1.5248
$j = 28$	0.4041	-0.394	-0.3417	-0.1744
$j = 29$	-7.8626	0.007	-0.0177	1.5665
$j = 30$	-1.9185	0.044	-0.0435	4.8126

TABLE B.2. Weights of the second hidden layer $w^2_{i,j}$ (30 × 30 matrix).

	$i = 1$	$i = 2$	$i = 3$	$i = 4$	$i = 5$	$i = 6$	$i = 7$	$i = 8$	$i = 9$	$i = 10$
$j = 1$	-0.0584	0.0718	0.2475	0.0422	0.0454	0.1838	0.2414	-0.1151	-0.2737	-0.1176
$j = 2$	0.0529	-0.0258	0.0089	-0.9330	-0.0879	0.1044	0.1184	-0.0830	-0.2109	0.1977
$j = 3$	-0.2396	0.0825	0.1115	0.1123	-0.3201	-0.0084	-0.1659	-0.0628	-0.0216	0.3037
$j = 4$	-0.4419	-0.4217	-0.0042	-0.0672	0.1651	-0.3884	0.1228	0.0901	-0.0971	0.0053
$j = 5$	0.1150	0.1003	0.2479	0.0020	-0.0917	-0.1650	-0.3353	0.0285	-0.0873	-0.0083
$j = 6$	-0.0404	-0.0245	-0.3185	0.2116	-0.8259	-0.0288	-0.1734	-0.0133	-0.5656	0.2325
$j = 7$	-0.0901	0.8309	-0.1453	0.8865	0.2757	0.2737	-0.0079	-0.1245	0.1366	0.1269
$j = 8$	-0.2214	-3.0984	-0.5174	-0.0558	0.2873	1.6477	0.0322	1.1222	0.6048	0.9131
$j = 9$	-0.1482	-0.0498	0.1908	-0.0228	0.2889	-0.1832	-0.3038	-0.3103	0.1912	-0.1617
$j = 10$	-0.3268	0.1031	-0.1708	0.4585	-0.2645	-0.3463	-0.3095	0.0986	0.1533	-0.2898
$j = 11$	-0.1602	-0.1897	0.1841	0.1298	0.2105	0.2729	-0.2597	0.0426	0.2721	-0.0004
$j = 12$	-0.1329	0.2737	-0.0467	-0.0258	-0.0219	-0.1008	0.2646	-0.0749	0.0759	0.1992
$j = 13$	0.2740	0.1452	0.2861	0.2451	0.0176	0.2099	0.0153	-0.1957	0.0268	0.0510
$j = 14$	-0.0955	0.2419	0.3990	0.0432	0.1711	-0.0813	-0.2527	-0.0466	-0.0407	-0.0395
$j = 15$	-0.2838	0.1437	-0.0143	-0.2083	-0.2008	0.1287	0.1910	-0.1617	0.0298	0.1815
$j = 16$	-0.0071	0.1291	0.2715	-0.1079	-2.1132	-0.0679	0.1791	0.0402	-0.1417	-0.0061

$j = 17$	-0.3664	-0.2941	-0.2582	0.1567	-2.4899	-0.0622	-0.0288	-0.2283	0.0675	0.0412
$j = 18$	0.0212	-0.1016	0.0143	-0.1632	0.1984	0.0467	-0.2130	-0.0380	0.2914	-0.1037
$j = 19$	-0.2418	0.1894	0.0864	-0.3889	0.0108	-0.0090	-0.3493	0.3966	-0.1945	0.1584
$j = 20$	-0.1646	0.0489	-0.5014	0.0302	-0.4817	-0.0126	-0.2973	-0.1877	-0.1952	-0.2024
$j = 21$	0.1894	0.2982	-0.1912	0.0147	0.1079	0.2432	-0.2127	0.1859	-0.1631	-0.2170
$j = 22$	-0.3818	0.3228	0.1250	-0.0418	0.0109	-0.2663	0.0535	-0.1296	-0.0266	0.4135
$j = 23$	-0.3439	-0.2162	-0.0614	-1.5111	0.0650	-1.7652	0.1159	0.1065	0.4084	-0.2060
$j = 24$	0.0940	-0.2438	0.6905	0.4834	-0.4044	0.2717	0.1450	-0.0211	-0.0090	0.0589
$j = 25$	0.0346	-0.1357	0.0440	-0.0988	-1.1211	-0.7743	-0.0203	-0.1804	-0.0668	0.0028
$j = 26$	0.1791	0.2591	0.0849	0.2750	0.2171	0.0728	-0.0531	0.2146	-0.2378	-0.2453
$j = 27$	-0.1144	-0.0830	0.1123	-0.2800	-0.0248	-0.0387	0.0937	-0.2302	-0.1153	-0.2550
$j = 28$	-0.2115	-0.0842	0.3041	-0.0350	-0.0238	0.0328	0.2844	0.2160	-0.1506	0.2875
$j = 29$	-0.4142	-0.1317	0.7627	-1.3978	0.2875	-0.4755	-0.2014	0.1141	0.1727	0.0097
$j = 30$	-0.0873	0.1265	0.1539	0.0743	0.4703	-0.0707	-0.1966	0.2529	0.0575	-0.2148

TABLE B.2. Weights of the second hidden layer $w^2_{i,j}$ (30 × 30 matrix). (cont.)

	$i = 11$	$i = 12$	$i = 13$	$i = 14$	$i = 15$	$i = 16$	$i = 17$	$i = 18$	$i = 19$	$i = 20$
$j = 1$	0.0018	-0.3680	0.2100	-0.1413	-0.0941	0.3079	0.0119	1.4304	0.2026	-2.4157
$j = 2$	0.1829	-0.1163	0.1285	-0.4309	0.0592	-0.9747	0.0120	0.2111	-0.8030	-2.2476
$j = 3$	-0.1398	-0.2171	-0.1992	-0.0077	0.0862	-0.4991	-0.0838	-0.5078	-1.3951	-0.7515
$j = 4$	-0.2955	0.2533	-0.2147	0.0971	-0.1827	-0.4714	-0.2871	-2.7332	0.4485	-0.2451
$j = 5$	0.1257	-0.1972	-0.2881	-0.2317	-0.0797	0.2369	-0.1035	0.0799	0.0710	-0.4256
$j = 6$	-0.3602	0.0169	-0.1359	0.7169	0.1530	-1.1324	-0.0290	-1.3050	-0.2134	-1.0745
$j = 7$	-0.0094	-1.1140	-0.1507	-0.0812	-1.6024	-2.2698	-0.2644	-0.0592	-0.0528	1.1621
$j = 8$	-0.2903	1.1746	-0.0657	0.6708	-0.2682	2.6619	-0.4020	0.6715	0.0859	0.2993
$j = 9$	-0.2562	0.3160	0.1353	-0.2243	-0.1446	0.0211	0.1829	0.1785	-0.0839	0.0068
$j = 10$	-0.3612	0.0059	-0.0039	-0.0358	0.1358	-0.0712	0.1213	0.1408	0.1321	0.1547
$j = 11$	-0.1126	0.0308	-0.2838	0.0418	-0.2965	0.2425	-0.1659	0.1687	-0.2153	-0.2515
$j = 12$	0.2791	0.0080	-0.1812	0.0669	-0.1985	-0.0639	-0.0982	-0.2457	0.1775	0.1153
$j = 13$	0.0262	-0.1379	0.2698	0.1862	-0.0840	0.2259	0.1124	0.0750	-0.1167	0.0838
$j = 14$	-0.1939	-0.1262	0.1914	-0.4919	0.1224	-0.0493	-0.0279	0.5224	0.4039	0.3652
$j = 15$	0.2592	0.0569	0.2471	0.2245	0.3123	0.2851	-0.0104	0.0409	-0.2375	0.1408
$j = 16$	0.0205	0.1193	0.0836	-0.0345	-0.0011	-0.1187	0.1719	-1.4886	-1.8825	-0.0352
$j = 17$	-0.3142	0.0201	-0.0675	-0.7679	0.3374	0.6984	0.1933	-3.0315	-0.5357	-1.9421
$j = 18$	0.2417	0.0366	0.0844	-0.1786	0.1661	-0.1431	-0.2633	0.0105	0.0235	0.1804
$j = 19$	-0.3457	0.7069	-0.0265	-0.1147	-0.3306	0.6932	-0.0191	0.1606	-0.3685	-0.5070
$j = 20$	0.0372	0.4800	-0.0723	-0.0059	-0.2654	-0.1362	-0.2128	-0.3559	0.6531	-0.3776
$j = 21$	-0.1244	0.0961	-0.2842	-0.1403	0.2916	0.0443	-0.1030	0.1440	-0.3110	0.0991
$j = 22$	-0.3081	0.0507	0.0896	-0.1104	-1.4292	0.1928	-0.3120	0.5701	-0.1939	0.5848
$j = 23$	0.2008	-0.5347	-0.3241	-0.2851	0.1529	-0.3383	-0.1496	-1.0224	-1.8450	-0.1005
$j = 24$	-0.0075	-0.2411	0.2319	0.2705	-0.1313	-2.0425	-0.0188	-1.4552	-0.1578	-0.6020
$j = 25$	-0.4318	-0.2362	-0.2397	-0.4148	0.0286	-0.0834	-0.1091	-0.4103	-0.5102	-0.0914
$j = 26$	-0.0020	0.1536	0.2922	0.0867	0.2047	0.0240	-0.0319	0.1272	0.0410	0.2805
$j = 27$	-0.0200	0.3192	-0.0367	0.0566	-0.0514	-0.3162	-0.2420	0.0775	0.0237	-0.2905
$j = 28$	0.0613	0.2910	-0.0079	0.0689	0.2698	-0.0405	0.2807	0.2494	0.0460	-0.0794
$j = 29$	0.1287	0.3261	-0.0980	0.1626	-0.2209	-3.6606	-0.4734	0.3828	-0.5779	0.8639
$j = 30$	0.1403	-0.2346	-0.0689	-0.1871	0.1808	-0.0210	0.2546	0.3281	-0.0671	0.3024

TABLE B.2. Weights of the second hidden layer $w^2_{i,j}$ (30 × 30 matrix). (cont.)

	$i = 21$	$i = 22$	$i = 23$	$i = 24$	$i = 25$	$i = 26$	$i = 27$	$i = 28$	$i = 29$	$i = 30$
$j = 1$	0.0869	0.0387	0.4551	-0.0359	-0.1926	-0.2417	0.2354	-0.0448	0.0214	0.3209
$j = 2$	-0.1841	0.0527	-0.0992	-0.0558	0.1502	-0.1861	0.1139	0.1223	-0.1205	-0.0131
$j = 3$	-0.2566	0.0535	-0.0594	0.0209	-0.3954	-0.0155	-0.1939	0.1719	-0.2129	0.3484
$j = 4$	-0.1690	-0.2609	-0.2549	-0.0851	-0.3848	-0.0134	0.1353	0.1017	0.0601	0.2062
$j = 5$	-0.0851	-0.1582	-0.2104	-0.0673	0.0911	-0.1537	-0.1686	0.0161	-0.0502	-0.2230
$j = 6$	0.0426	0.0963	0.3194	-0.1196	-0.0039	-0.2038	0.1850	-0.0903	0.1215	0.2001
$j = 7$	0.2266	0.2895	0.2393	-0.1636	-0.0081	0.1253	-0.7818	0.9140	-0.2862	0.1758
$j = 8$	-0.0580	1.0213	0.3030	-0.9736	0.7444	0.0134	-0.7905	-0.9841	-0.0146	-0.6309
$j = 9$	0.2768	-0.0908	-0.1599	-0.2834	0.0135	-0.2507	0.0143	0.1389	0.0044	-0.1064
$j = 10$	-0.1300	-0.1723	0.1180	0.0378	0.1364	-0.2209	0.5092	-0.0285	-0.0638	-0.1679
$j = 11$	0.1052	0.1965	0.0482	-0.1289	-0.1618	0.1928	0.1919	0.1674	-0.0473	0.0637
$j = 12$	0.1436	0.1183	0.2206	-0.2024	0.1258	0.2298	-0.1916	-0.2192	-0.0378	-0.1465
$j = 13$	0.2079	-0.1247	-0.0326	0.0926	0.2724	0.2880	0.1897	0.0002	-0.0852	-0.2514
$j = 14$	0.2611	-0.0273	0.3781	-0.0094	-0.4060	0.0764	-0.2543	0.0122	0.2847	-0.3051
$j = 15$	-0.1571	0.2923	0.1963	0.1600	0.1253	0.0024	-0.1707	-0.2829	-0.0127	0.1590
$j = 16$	0.0678	0.1820	-0.2898	0.0351	-3.5119	0.2366	-0.0178	-0.0396	-0.1544	-0.1436
$j = 17$	-0.2678	-0.1883	-1.2206	-0.1182	-1.3145	-0.2448	0.0571	-0.0084	0.0008	0.9046
$j = 18$	-0.0951	0.2709	-0.1425	-0.0410	-0.0377	0.2074	-0.1492	0.1614	-0.3085	-0.1445
$j = 19$	0.0235	-0.2800	-0.1302	-0.1531	-0.2068	-0.4006	-0.3529	0.0069	-0.2070	0.1246
$j = 20$	-0.1484	0.1757	0.1663	-0.1993	0.2246	-0.2242	0.0460	-0.0969	-0.1247	0.5174
$j = 21$	-0.2637	-0.1279	0.0838	0.0747	-0.2897	-0.1745	0.0305	0.0390	-0.0674	-0.2028
$j = 22$	-0.3099	0.4254	0.6193	0.0379	0.2141	0.0287	0.5318	0.0214	-0.0525	-0.3993
$j = 23$	-0.1177	-0.0647	0.0991	-0.2402	-0.4760	-0.1553	-0.6934	0.2604	-0.0352	-0.4313
$j = 24$	-0.0850	0.2562	0.1537	0.0891	-0.3783	-0.0210	0.5584	-0.3127	-0.2128	0.0318
$j = 25$	-0.0645	0.2279	-0.0181	-0.1425	0.1057	-0.5575	-0.1670	0.1717	-0.3330	-0.0789
$j = 26$	0.0294	-0.2920	0.0172	-0.2095	-0.0259	0.1946	0.0233	-0.0056	-0.0558	-0.3027
$j = 27$	-0.2644	0.2442	0.2604	0.1276	0.0486	0.0006	0.0868	0.2102	-0.2184	-0.0073
$j = 28$	0.2741	0.0570	0.1332	-0.2582	0.1392	-0.2367	-0.2972	-0.1669	0.1820	0.1558
$j = 29$	0.0127	0.1388	0.0053	-0.1195	-3.4818	-0.3500	-0.8159	0.1197	-0.3818	-0.9309
$j = 30$	0.1058	-0.1209	0.0105	0.0180	0.0733	0.0078	-0.1221	-0.1254	-0.0267	-0.3089

TABLE B.3. Weights of the output layer $w^3_{i,j}$ (30 × 1 matrix).

	$j = 1$
$i = 1$	-0.0238
$i = 2$	0.0758
$i = 3$	-0.0922
$i = 4$	-0.1659
$i = 5$	0.0635
$i = 6$	0.1569
$i = 7$	-0.1470
$i = 8$	0.0456
$i = 9$	0.0518
$i = 10$	0.1929
$i = 11$	-0.0532
$i = 12$	0.0664
$i = 13$	0.1428
$i = 14$	-0.0299
$i = 15$	0.0625
$i = 16$	-0.0568

$i = 17$	-0.0067
$i = 18$	0.1170
$i = 19$	0.0438
$i = 20$	0.1290
$i = 21$	-0.1040
$i = 22$	0.0869
$i = 23$	0.0455
$i = 24$	0.0208
$i = 25$	-0.1761
$i = 26$	0.0826
$i = 27$	0.0695
$i = 28$	-0.0984
$i = 29$	0.0046
$i = 30$	-0.0685

TABLE B.4. Biases of the first hidden layer $b^1_{i,j}$ (1 × 30 matrix), second hidden layer $b^2_{i,j}$ (1 × 30 matrix), and output layer $b^3_{i,j}$ (1 × 1 matrix).

	$b^1_{i,j}$ ($i = 1$)	$b^2_{i,j}$ ($i = 1$)	$b^3_{i,j}$ ($i = 1$)
$j = 1$	-2.4199	-0.1980	0.9022
$j = 2$	-0.2416	0.7119	
$j = 3$	-0.1135	-0.8390	
$j = 4$	-0.5961	-1.8977	
$j = 5$	-0.3848	-0.4000	
$j = 6$	-0.4754	-1.4210	
$j = 7$	-0.0649	-0.2164	
$j = 8$	0.5372	0.7572	
$j = 9$	0.0000	1.2333	
$j = 10$	2.4306	1.0627	
$j = 11$	0.0000	-0.1835	
$j = 12$	0.0000	0.3836	
$j = 13$	0.0000	-0.0603	
$j = 14$	-0.8687	0.5920	
$j = 15$	0.0000	1.3056	
$j = 16$	1.5574	-0.7386	
$j = 17$	-1.6345	-1.0443	
$j = 18$	0.0000	0.5531	
$j = 19$	1.7000	0.4785	
$j = 20$	2.1082	0.2225	
$j = 21$	0.0000	0.0000	
$j = 22$	1.4032	1.1514	
$j = 23$	-1.0942	0.8386	
$j = 24$	1.6302	-0.7953	
$j = 25$	-0.1536	0.1870	
$j = 26$	-0.0021	-0.2918	
$j = 27$	-0.3134	1.1543	
$j = 28$	0.0000	-2.0475	
$j = 29$	2.1984	-0.1549	
$j = 30$	-1.2092	-0.6425	

DATA AVAILABILITY STATEMENTS

The data that support the findings of this study are available from the corresponding author, S. Shin, upon reasonable request.

References

1. D. Lohse, “Fundamental fluid dynamics challenges in inkjet printing,” Annu. Rev. Fluid Mech. **54**, 349–382 (2021).

2. R. Daly, T. S. Harrington, G. D. Martin, and I. M. Hutchings, “Inkjet printing for pharmaceutics—A review of research and manufacturing,” Int. J. Pharm. **494** (2), 554–567 (2015).

3. S. Yun, “Controlling the rebound on a solid surface by varying impact angles of ellipsoidal drops,” Phys. Fluids **33**, 042105 (2021).

4. C. Ukiwe and D. Y. Kwok, “On the maximum spreading diameter of impacting droplets on well-prepared solid surfaces,” Langmuir **21**, 2, 666–673 (2005).

5. N. Lann, K. G. Bruin, D. Slenter, J. Wilhelm, M. Jermy, and D. Bonn, “Bloodstain pattern analysis: Implementation of a fluid dynamic model for position determination of victims,” Sci. Rep. **5**, 11461 (2015).

6. A. Marmur, “The lotus effect: Superhydrophobicity and metastability,” Langmuir **20** (9), 3517–3519 (2004).

7. E. Teunou, and D. Poncelet, "Batch and continuous fluid bed coating – review and state of the art," Journal of Food Engineering, **53** (4), 325-340 (2002).

8. D. A. Bolleddula, A. Berchielli and A. Aliseda, "Impact of a heterogeneous liquid droplet on a dry surface: Application to the pharmaceutical industry," Advances in Colloid and Interface Science, **159** (2) 144-159 (2010).

9. C. Josserand and S. T. Thoroddsen, “Drop impact on a solid surface,” Annu. Rev. Fluid Mech. **48**, 365–391 (2016).

10. M. Marengo, C. Antonini, I. V. Roisman, and C. Tropea, “Drop collisions with simple and complex surfaces,” Curr. Opin. Colloid Interface Sci. **16** (4), 292–302 (2011).

11. T. Mao, D. Kuhn, and H. Tran, “Spread and rebound of liquid droplets upon impact on flat surfaces,” AIChE J. **43**, 2169–2179 (1997).

12. C. Clanet, C. Béguin, D. Richard, and D. Quéré, “Maximal deformation of an impacting drop,” J. Fluid Mech. **517**, 199–208 (2004).

13. J. B. Lee, N. Laan, K. G. De Bruin, G. Skantzaris, N. Shahidzadeh, D. Derome, J. Carmeliet, and C. Bonn, “Universal rescaling of drop impact on smooth and rough surfaces,” J. Fluid Mech. **786**, R4 (2016).

14. S. Wildeman, C. Visser, C. Sun, and D. Lohse, “On the spreading of impacting drops,” J. Fluid Mech. **805**, 636–655 (2016).

15. C. Antonini, A. Amirfazli, and M. Marengo, “Drop impact and wettability: From hydrophilic to superhydrophobic surfaces,” Phys. Fluids **24**, 102104 (2012).

16. R. Rioboo, M. Marengo, and C. Tropea, “Time evolution of liquid drop impact onto solid, dry surfaces,” Exp. Fluids **33**, 112–124 (2002).

17. I.V. Roisman, L. Opfer, C. Tropea, M. Raessi, J. Mostaghimi, and S. Chandra, “Drop impact onto a dry surface: Role of the dynamic contact angle,” Colloids Surf. **322** (1–3), 183–191 (2008).

18. R. Rioboo, C. Tropea, and M. Marengo, “Outcomes from a drop impact on solid surface,” Atomization Spray. **11** (2), 155–165 (2001).

19. I. V. Roisman, “Inertia dominated drop collisions. II. An analytical solution of the Navier–Stokes’s equations for a spreading viscous film,” Phys. Fluids **21**, 052104 (2009).

20. J. Eggers, M. A. Fontelos, C. Josserand, and S. Zaleski, “Drop dynamics after impact on a solid wall: Theory and simulations,” Phys. Fluids **22**, 062101 (2010).

21. X. Liu, H. Chen, S. Chen, S. Shen, and X. Zhao, “Research progress of droplet impact on dry curve surfaces,” AIP Conf. Proc. **1984**, 020036 (2018).

22. D. Khojasteh, N. M. Kazerooni, and M. Marengo, “A review of liquid droplet impacting onto solid spherical particles: A physical pathway to encapsulation mechanisms,” J. Ind. Eng. Chem. **71**, 50–64 (2019).

23. S. Bakshi, I. V. Roisman, and C. Tropea, “Investigations on the impact of a drop onto a small spherical target,” Phys. Fluids **19**, 032102 (2007).

24. Y. Zhu, H. Liu, K. Mu, P. Gao, H. Ding, and X. Lu, “Dynamics of drop impact onto a solid sphere: Spreading and retraction.” J. Fluid Mech. **824**, R3 (2017).

25. S. Mitra, G. M. Evans, E. Doroodchi, V. Pareek, and J. B. Joshi, “Interactions in droplet and particle system of near unity size ratio,” Chem. Eng. Sci. **170**, 154–175 (2017).

26. S. A. Banitabaei and A. Amirfazli, “Droplet impact onto a solid sphere: Effect of wettability and impact velocity,” Phys. Fluids **29**, 062111 (2017).

27. S. A. Banitabaei and A. Amirfazli, “Droplet impact onto a solid sphere in midair: Effect of viscosity, gas density, and diameter ratio on impact outcomes,” Phys. Fluids 32, 037102 (2020).

28. V. Vilela, F. J. de Souza, "A Numerical Study on Droplet-Particle Collision," Flow Turbulence Combust 105, 965–987 (2020).

29. I. Yoon and S. Shin, “Direct numerical simulation of droplet collision with stationary spherical particle: A comprehensive map of outcomes,” Int. J. Multiph. Flow **135**, 103503 (2021).

30. H. N. Dalgamoni and X. Yong, "Numerical and theoretical modeling of droplet impact on spherical surfaces," Phys. Fluids **33**, 052112 (2021).

31. I. Malgarinos, N. Nikolopoulos, and M. Gavaises, "Numerical investigation of heavy fuel droplet-particle collisions in the injection zone of a Fluid Catalytic Cracking reactor, Part I: Numerical model and 2D simulations,", Fuel Processing Technology 156, 317-330 (2017).

32. I. Malgarinos, N. Nikolopoulos, and M. Gavaises, "Numerical investigation of heavy fuel droplet-particle collisions in the injection zone of a Fluid Catalytic Cracking reactor, part II: 3D simulations,", Fuel Processing Technology 156, 43-53 (2017).

33. S. Mitra, M. J. Sathe, E. Doroodchi, R. Utikar, M. K. Shah, V. Pareek, J. B. Joshi, and G. M. Evans, “Droplet impact dynamics on a spherical particle,” Chem. Eng. Sci. **100**, 105–119 (2013).

34. S. Mitra and G. M. Evans, “Dynamic surface wetting and heat transfer in a droplet-particle system of less than unity size ratio,” Front. Chem. **6**, 259 (2018).

35. Y. P. Li and H. R. Wang, “Three-dimensional direct simulation of a droplet impacting onto a solid sphere with low-impact energy,” Can. J. Chem. Eng. **89**, 83–91 (2011).

36. X. Liu, X. Zhang, and J. Min, “Maximum spreading of droplets impacting spherical surfaces,” Phys. Fluids. **31**, 092102 (2019).

37. I. Yoon and S. Shin, “Computational study on dynamic behavior during droplet-particle interaction,” Chem. Eng. Sci. **241**, 116656 (2021).

38. G. Khurana, N. Sahoo, and P. Dhar, “Phenomenology of droplet collision hydrodynamics on wetting and non-wetting spheres,” Phys. Fluids **31**, 072003 (2019).

39. S. Mitra, T. B. T. Nguyen, E. Doroodchi, V. Pareek, J. B. Joshi, and G. M. Evans, “On wetting characteristics of droplet on a spherical particle in film boiling regime,” Chem. Eng. Sci. **149**, 181–203 (2016).

40. D. Khojasteh, A. Bordbar, R. Kamali, and M. Marengo, “Curvature effect on droplet impacting onto hydrophobic and superhydrophobic spheres,” Int. J. Comput. Fluid Dynam. **31**, 310–323 (2017).

41. A. Bordbar, A. Taassob, D. Khojasteh, M. Marengo, and R. Kamali, “Maximum spreading and rebound of a droplet impacting onto a spherical surface at low weber numbers,” Langmuir **34**, 5149–5158 (2018).

42. I. Yoon and S. Shin, “Maximal spreading of droplet during collision on particle: effects of liquid viscosity and surface curvature,” Phys. Fluids **33**, 083310 (2021).

43. G. H. McKinley and M. Renardy, “Wolfgang von Ohnesorge,” Phys. Fluids. **23**, 127101 (2011).

44. B. Derby, “Inkjet printing of functional and structural materials: Fluid property requirements, feature stability and resolution,” Annu. Rev. Mater. Res. 40, 395 (2010).

45. F. Gao and A. A. Sonin, “Precise deposition of molten microdrops: the physics of digital microfabrication,” Proc. R. Soc. Lond. A **444**, 533–554 (1994).

46. Y. Ge and L. Fan, “Droplet–particle collision mechanics with film-boiling evaporation,” J. Fluid Mech. **573**, 311–337 (2007).

47. I. Yoon, J. Chergui, D. Juric, and S. Shin, “Adaptive mesh axi-symmetric simulation of droplet impact with a spherical particle in mid-air,” Int. J. Multiph. Flow **XXX**, 104193 (2022).

48. S. Shin, and D. Juric, “Modeling three-dimensional multiphase flow using a level contour reconstruction method for front tracking without connectivity,” J. Comput. Phys. **180**, 427–470 (2002).

49. S. Shin and D. Juric, “A hybrid interface method for three-dimensional multiphase flows based on front tracking and level set techniques,” Int. J. Numer. Meth. Fluids **60,** 753–778 (2009).

50. S. Shin, J. Chergui, and D. Juric, “Direct simulation of multiphase flows with modeling of dynamic interface contact,” Theor. Comput. Fluid Dyn. **32**, 655–687 (2018).

51. J. Han, W. Kim, C. Bae, D. Lee, S. Shin, Y. Nam, and C. Lee, "Contact time on curved superhydrophobic surfaces," Phys. Rev. E **101**, 043108 (2020)**.**

52. S. Shin, J. Chergui, and D. Juric, "A solver for massively parallel direct numerical simulation of three-dimensional multiphase flows," J. Mech. Sci. Technol. **31**, 1739–1751 (2017).

53. S. Unverdi, and G. Tryggvason, "A front-tracking method for viscous, incompressible, multi-fluid flows," J. Comput. Phys. **100**, 25–37 (1992).

54. S. Osher and J. Sethian, "Fronts propagating with curvature-dependent speed: Algorithms based on Hamilton-Jacobi formulations," J. Comput. Phys. **79**, 12–49 (1988).

55. Y. Hardalupas, A. M. K. P. Taylor and J. H. Wilkins, "Experimental investigation of sub-millimetre droplet impingement on to spherical surfaces," Int. J. Heat Fluid Flow **20** (5), 477–485 (1999).

56. B. R. Munson, D. F. Young, and T. H. Okiishi, *Fundamentals of Fluid Mechanics*, 5th ed. (John Wiley and Sons, New York, 2006).

57. M. Pasandideh-Fard, S. Chandra, and J. Mostaghimi, "A three-dimensional model of droplet impact and solidification," Int. J. Heat Mass Transf. **45**, 2229–2242 (2002).

58. X. Liu, J. Min, X. Zhang, Z. Hu and X. Wu, "Supercooled water droplet impacting-freezing behaviors on cold superhydrophobic spheres," Int. J. Multiph. Flow **141**, 103675 (2021).

59. D. Bartolo, C. Josserand, and D. Bonn, “Retraction dynamics of aqueous drops upon impact on non-wetting surfaces”, J. Fluid Mech. **545**, 329–338 (2005).

60. M. Ma, J. Lu, and G. Tryggvason, "Using statistical learning to close two-fluid multiphase flow equations for a simple bubbly system," Phys. Fluids. **27**, 092101 (2015).

61. K. Fukami, K. Fukagata, and K. Taira, “Assessment of supervised machine learning methods for fluid flows,” Theor. Comput. Fluid Dyn. **34**, 497–519 (2020).

62. X. Jin, P. Cheng, W. Chen, and H. Li, "Prediction model of velocity field around circular cylinder over various Reynolds numbers by fusion convolutional neural networks based on pressure on the cylinder," Phys. Fluids. **30**, 047105 (2018).

63. R. Han, Y. Wang, Y. Zhang, and G. Chen, "A novel spatial-temporal prediction method for unsteady wake flows based on hybrid deep neural network," Phys. Fluids. **31**, 127101 (2019).

64. V. Sekar, Q. Jiang, C. Shu, and B. C. Khoo, "Fast flow field prediction over airfoils using deep learning approach," Phys. Fluids. **31**, 057103 (2019).

65. P. Hadikhani, N. Borhani, S. M. H. Hashemi, and D. Psaltis, “Learning from droplet flows in microfluidic channels using deep neural networks,” Sci Rep **9**, 8114 (2019).

66. F. Gibou, D. Hyde, and R. Fedkiw,"Sharp interface approaches and deep learning techniques for multiphase flows," J. Comput. Phys., **380**, 442-463 (2019).

67. F. Rosenblatt, “The Perceptron, a perceiving and recognizing automaton project para,” Report Vol. 85, Nos. 460–461, Cornell Aeronautical Laboratory, 1957

68. D. E. Rumelhart, G. E. Hinton, and R. J. Williams, “Neurocomputing: Foundations of Research, Learning Representations by Back-propagating Errors” MIT Press (Cambridge, MA, USA, 1988), 696–699

69. V. Nair, and G. E. Hinton, “Rectified linear units improve restricted Boltzmann machines,” In: Proceedings of 27th International Conference on Machine Learning (2010)

70. D. P. Kingma and J. Ba, “Adam: A method for stochastic optimization,” presented at the Third International Conference on Learning Representations, San Diego, CA, USA, 2015; e-print arXiv:1412.6980

71. S. Ruder, “An overview of gradient descent optimization algorithms,” [cs.LG], 2017.

72. Abadi, M. *et al.*, “TensorFlow: Large-scale machine learning on heterogeneous systems,” Software available from https://www.tensorflow.org/, 2015.

73. F. Chollet, “Keras,” (2015), https://keras.io.

74. M. A. Nielsen, “Neural Network and Deep Learning,” Determination Press (2015).

75. P. Attané, F. Girard, v. Morin, “An energy balance approach of the dynamics of drop impact on a solid surface,” Phys. Fluids **19**, 012101 (2007).

76. K. Yokoi, D. Vadillo, J. Hinch, and I. Hutchings, “Numerical studies of the influence of the dynamic contact angle on a droplet impacting on a dry surface,” Phys. Fluids **21**, 072102 (2009).

FIGURES

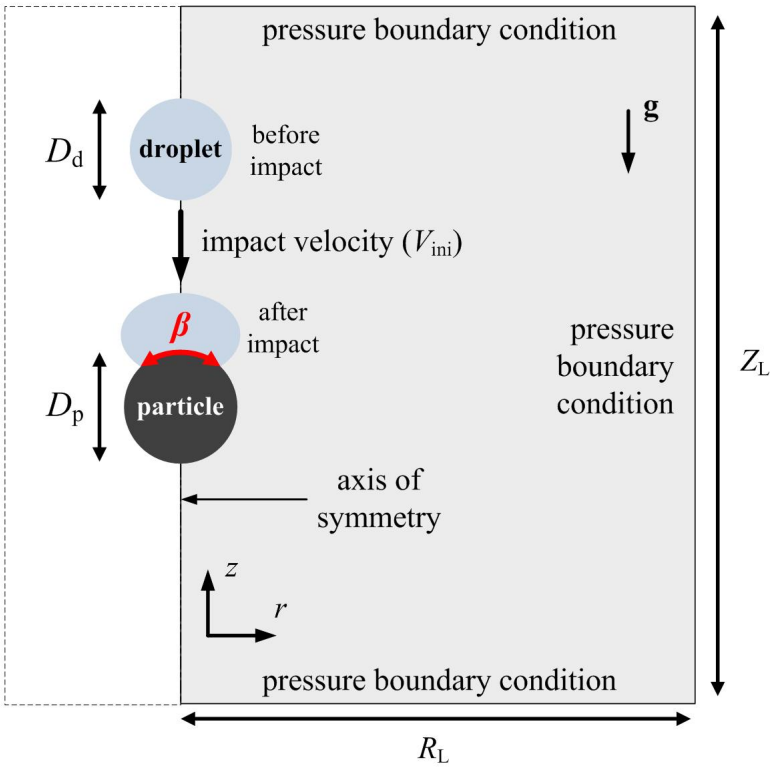

Fig. 1. Simulation domain and boundary conditions for droplet-particle collision system.

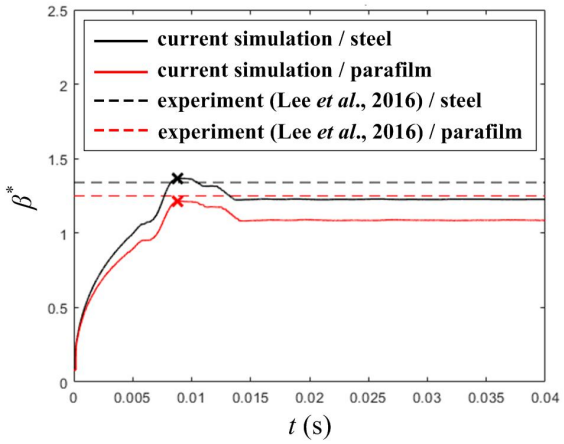

(a)

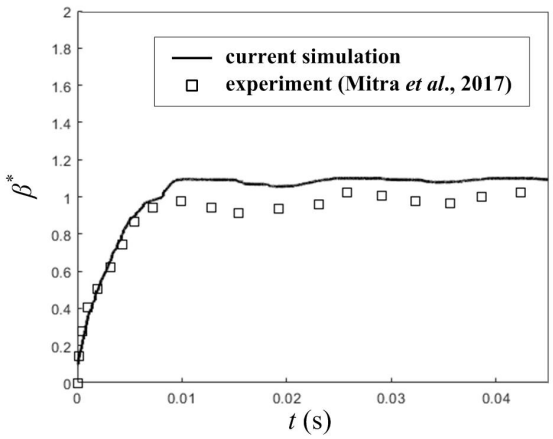

(b)

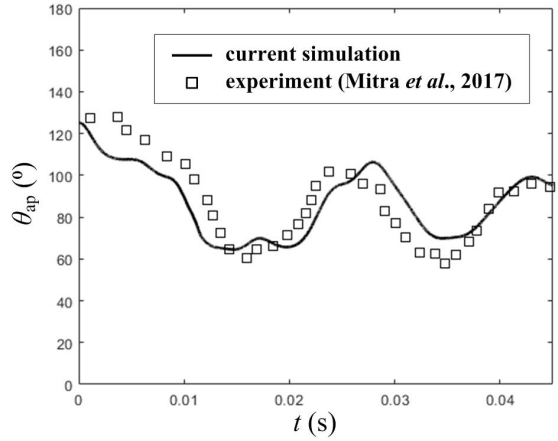

(c)

Fig. 2. Benchmarking comparison between existing results and current simulation results. (a) Comparison with the experimental result of Lee *et al.*[13] for droplet impact with a flat surface (We = 0). (b) Comparison of the nondimensional spreading diameter (β^*) with the experimental result of Mitra *et al.*[25] for droplet impact with a spherical particle (We = 0.9, Ω = 0.89, θ_{eqi} = 85°). (c) Comparison of the apparent contact angle with the experimental result of Mitra *et al.*[25] All impact conditions are the same as Fig.2 (b).

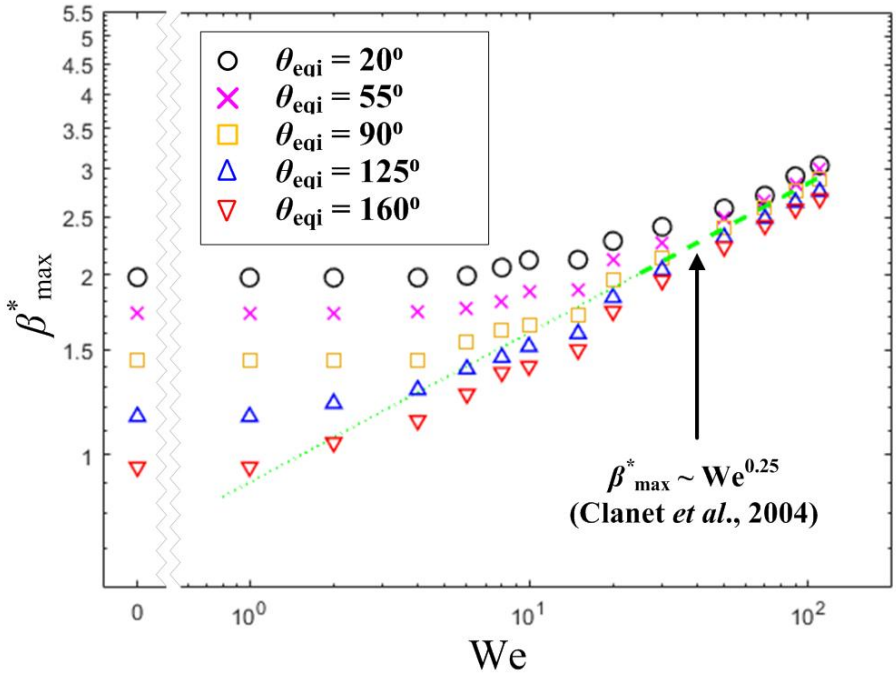

Fig. 3. Effect of Weber number (We) and surface wettability (θ_{eqi}) on the maximum spreading diameter (β^*_{max}). The existing scaling relation of Clanet *et al.*[12] is indicated by the green dashed line. Oh = 0.0026, Ω = 1/10.

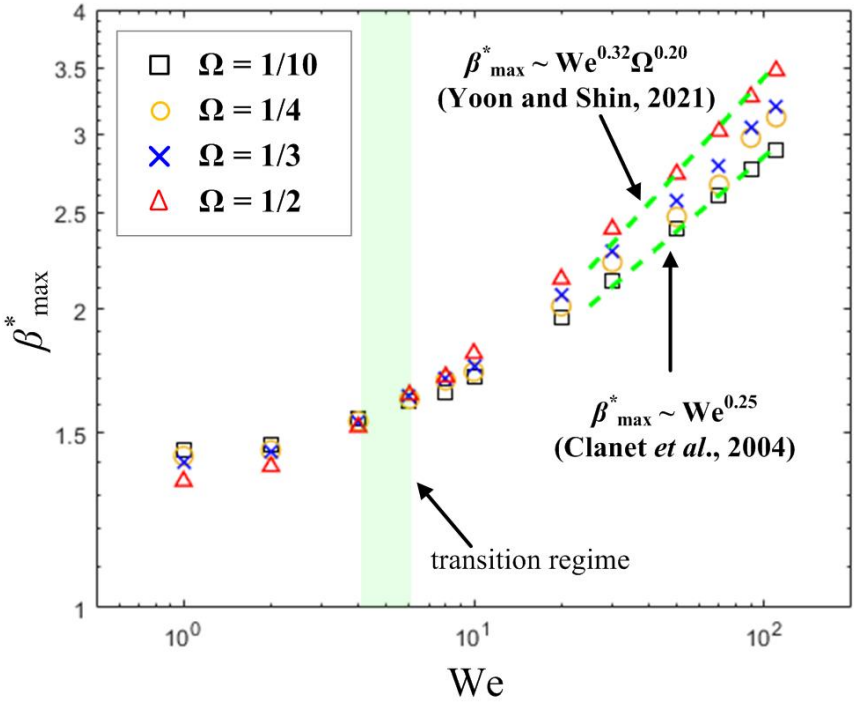

Fig. 4. Effect of droplet-to-particle diameter ratio (Ω) on the maximum spreading diameter (β^*_{max}) for a Weber number range of $1 \leq We \leq 110$. The existing scaling relations of Clanet *et al.*[12] and Yoon and Shin[42] are indicated by two green dashed lines. Oh = 0.0026, $\theta_{eqi} = 90°$.

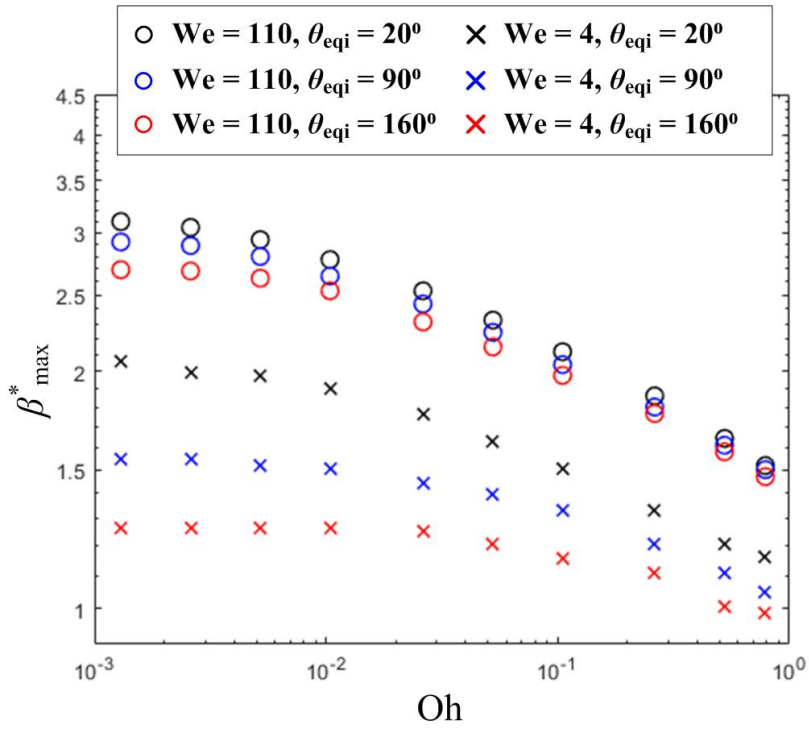

Fig. 5. Effect of surface wettability (θ_{eqi}) on the maximum spreading diameter (β^*_{max}) for an Ohnesorge number range of $0.0013 \leq Oh \leq 0.7869$. The cases with We = 110 and We = 4 are plotted for the high and low Weber number regimes, respectively. $\Omega = 1/10$.

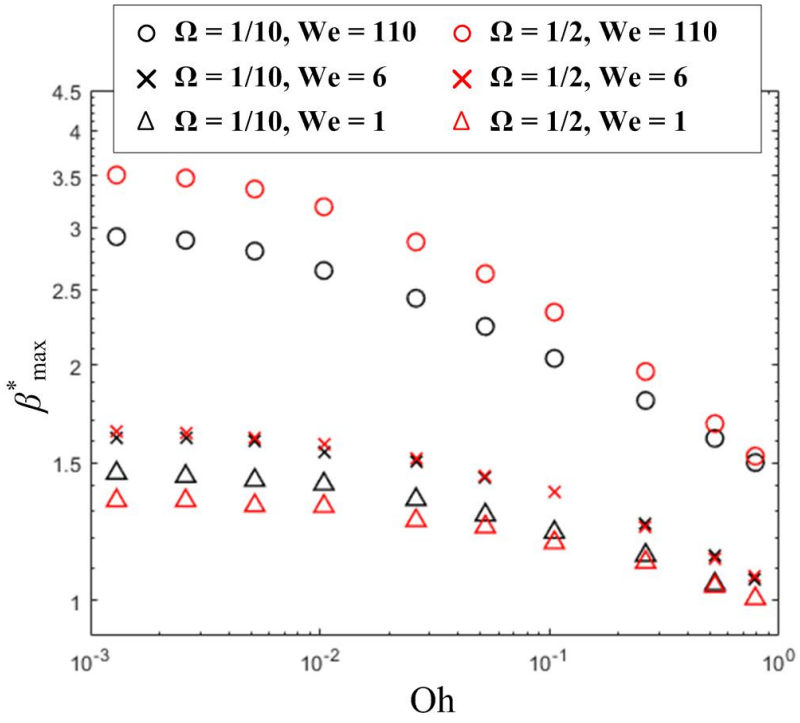

Fig. 6. Effect of droplet-to-particle diameter ratio (Ω) on the maximum spreading diameter (β^*_{max}) for an Ohnesorge number range of $0.0013 \leq Oh \leq 0.7869$. The cases with We = 110, We = 4, and We = 1 are plotted for the high Weber number regime, transition regime, and low Weber number regimes, respectively. $\theta_{eqi} = 90°$.

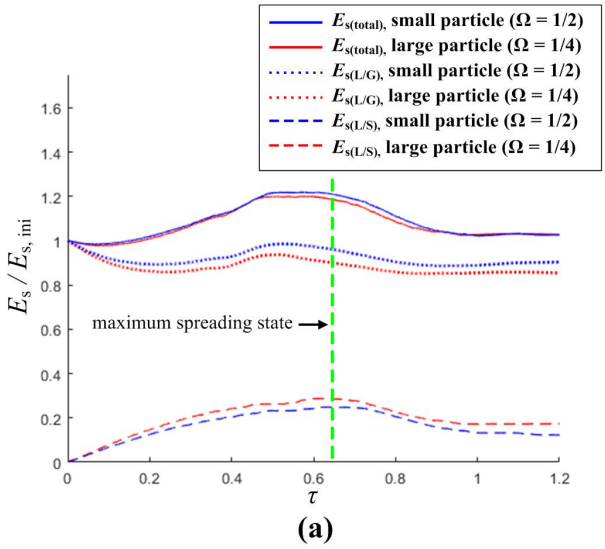

(a)

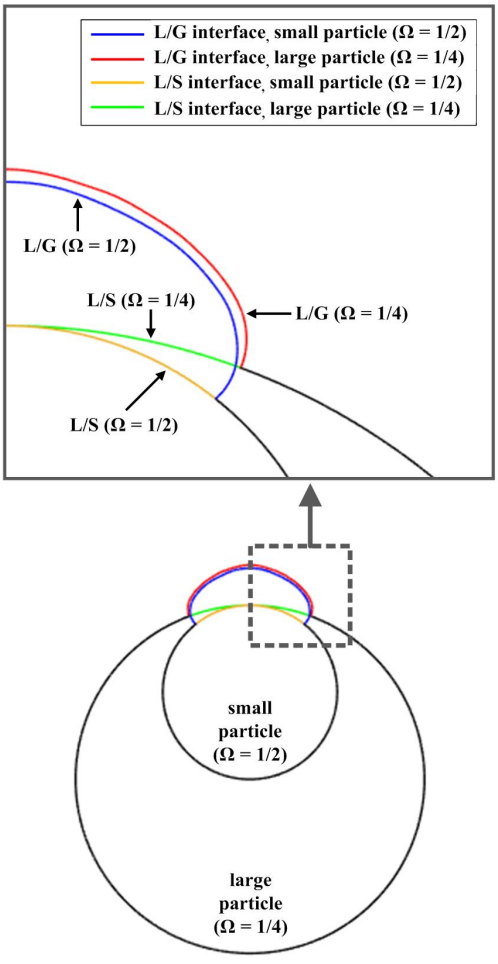

(b)

Fig. 7. (a) Comparison of two different surface energy components, i.e., $E_{s(L/G)}$ and $E_{s(L/S)}$, and the total surface energy between Ω = 1/4 (red lines) and 1/2 (blue lines). All variables are normalized by the initial total surface energy $E_{s,ini}$. The green dashed line indicates the maximum spreading state. (b) Comparison of liquid-gas interfacial shape between Ω = 1/4 (red line) and 1/2 (blue line). Liquid-solid contact areas are also marked by green (Ω = 1/4) and yellow line (Ω = 1/2).

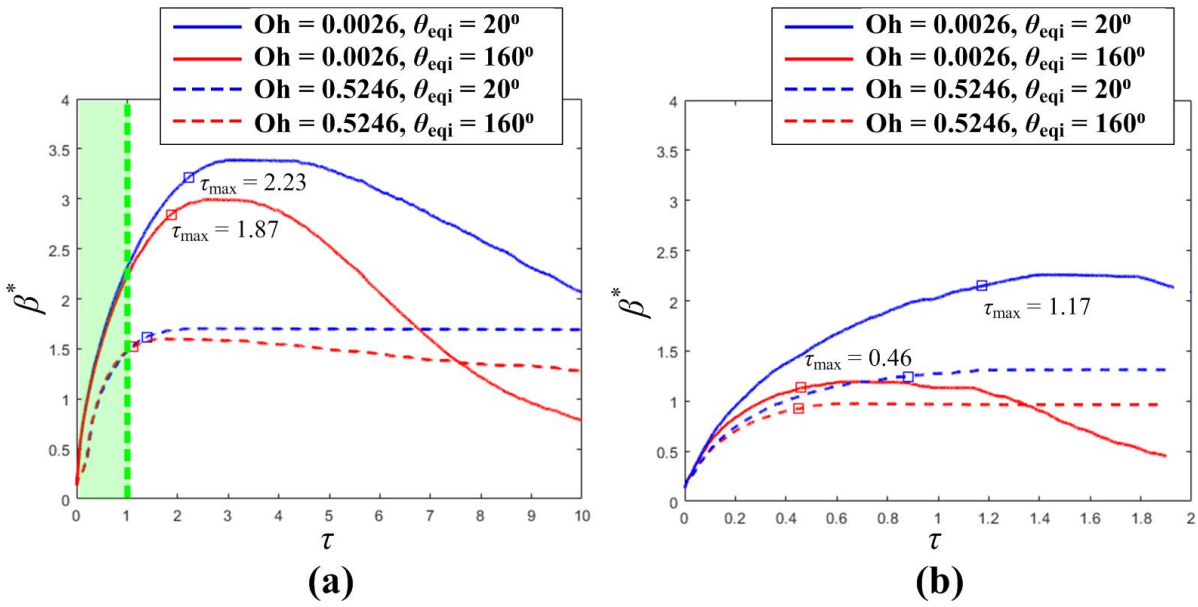

Fig. 8. Temporal evolution of the nondimensional spreading diameter (β^*). (a) We =110. Green dashed line and green area indicate $\tau = 1$ and the initial period ($0 \leq \tau \leq 1$), respectively. At this initial period, β^* shows an identical profile regardless of θ_{eqi}, under the given Oh condition. (b) We = 4.

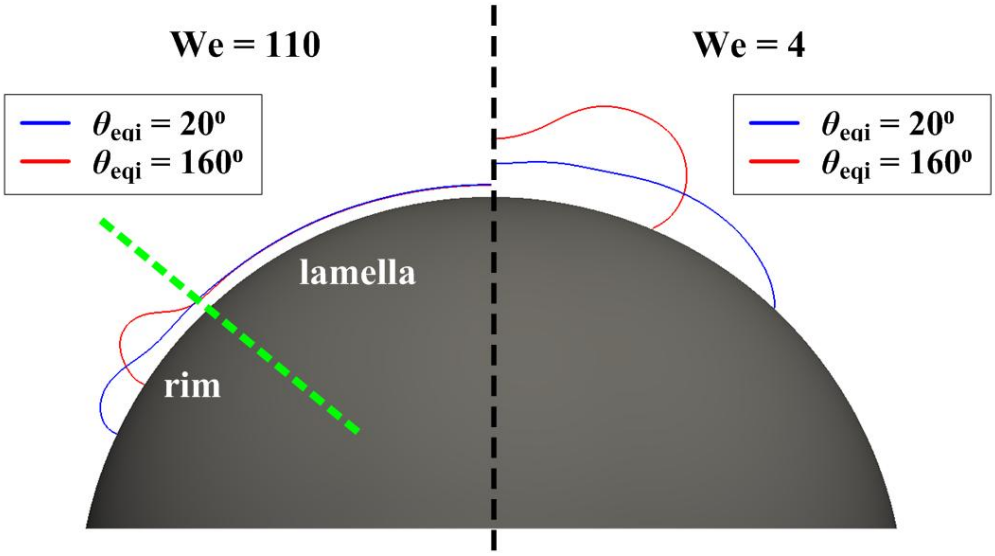

Fig. 9. Comparison of interfacial morphologies at the maximum spreading state between We = 110 (left side) and We = 4 (right side). Green dashed line on the left side indicates the conceptual boundary between the lamella and rim.

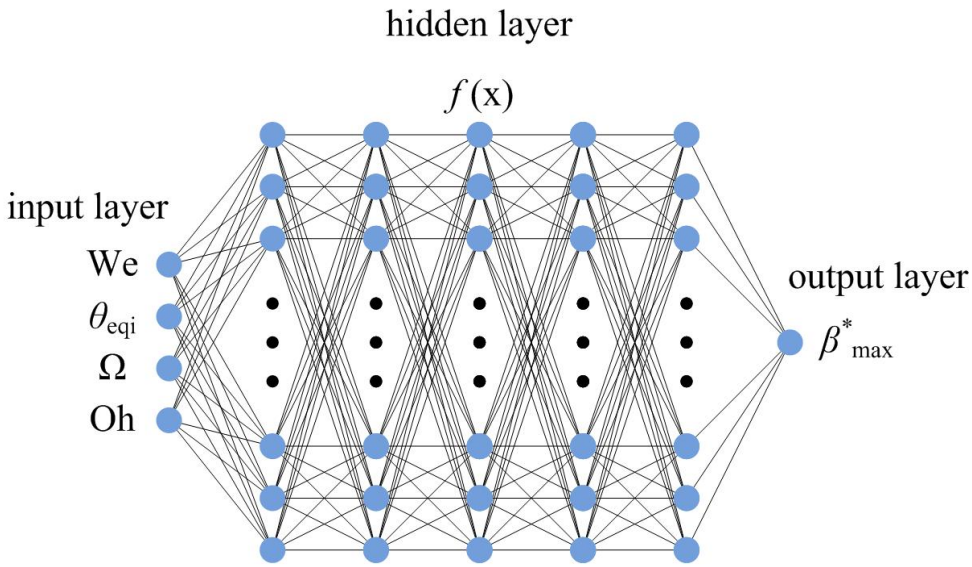

Fig. 10. Schematic architecture of the multilayer perceptron (MLP) applied in the present study.

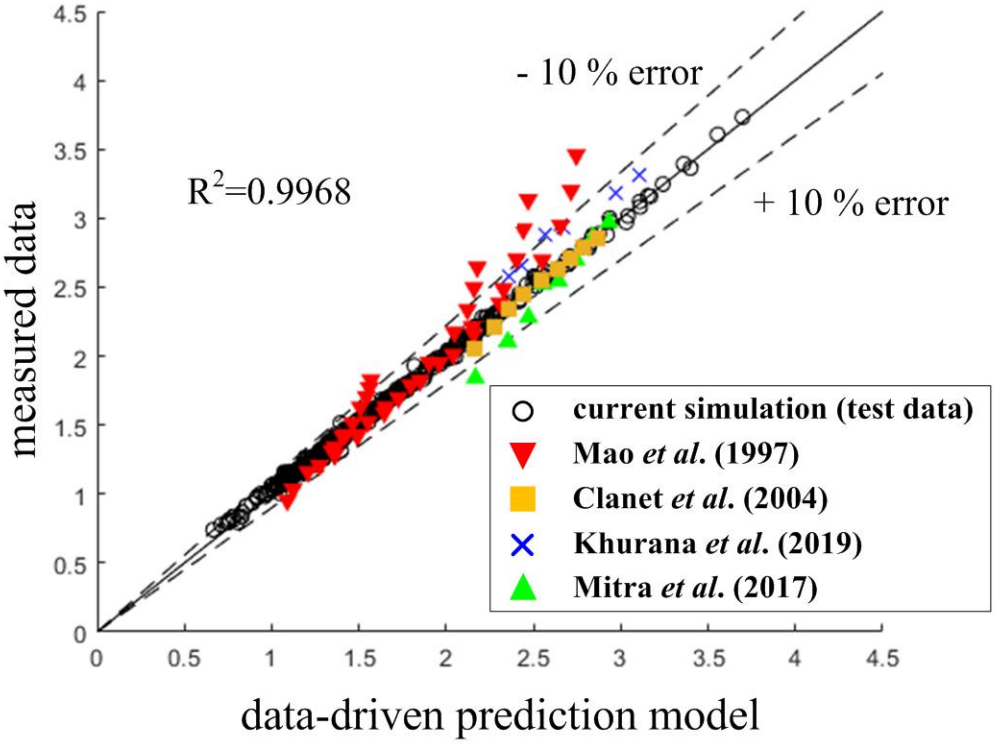

Fig. 11. Comparison of maximum spreading diameter of droplet β^*_{max} between measured (true) data obtained by our numerical simulations and predicted data using the deep neural network. The deviation range of ± 10% is indicated by the two dashed-black lines. 4 existing results of Mao *et al.*,[11] Clanet *et al.*,[12] Khurana *et al.*[38] and Mitra *et al.*[25] are also plotted for comparison.